# Investigation of polymers as functional layers of a light actuated digital microfluidic device

Henri van Eetveldt

Thesis presented in fulfilment of the requirements for the degree of Master of Engineering (Research) in the Faculty of Engineering at Stellenbosch University.

Supervisor: Prof W. J. Perold

Department of Electrical and Electronic Engineering

Co-supervisor: Prof C. Schutte

Department of Industrial Engineering

March 2021

# Acknowledgements

I would like to thank my parents, Frans and Elona for giving me the opportunity to study. I also would like to thank Zsa, for providing extra care while my time was needed elsewhere. Finally, I would like to thank Prof Willie Perold, for unyielding trust in me and my abilities to finish this project.

# Plagiaatverklaring / *Plagiarism Declaration*

1. Plagiaat is die oorneem en gebruik van die idees, materiaal en ander intellektuele eiendom van ander persone asof dit jou eie werk is.
   *Plagiarism is the use of ideas, material and other intellectual property of another's work and to present is as my own.*

2. Ek erken dat die pleeg van plagiaat 'n strafbare oortreding is aangesien dit 'n vorm van diefstal is.
   *I agree that plagiarism is a punishable offence because it constitutes theft.*

3. Ek verstaan ook dat direkte vertalings plagiaat is.
   *I also understand that direct translations are plagiarism.*

4. Dienooreenkomstig is alle aanhalings en bydraes vanuit enige bron (ingesluit die internet) volledig verwys (erken). Ek erken dat die woordelikse aanhaal van teks sonder aanhalingstekens (selfs al word die bron volledig erken) plagiaat is.
   *Accordingly all quotations and contributions from any source whatsoever (including the internet) have been cited fully. I understand that the reproduction of text without quotation marks (even when the source is cited) is plagiarism*

5. Ek verklaar dat die werk in hierdie skryfstuk vervat, behalwe waar anders aange-dui, my eie oorspronklike werk is en dat ek dit nie vantevore in die geheel of gedeeltelik ingehandig het vir bepunting in hierdie module/werkstuk of 'n ander module/werkstuk nie.
   *I declare that the work contained in this assignment, except where otherwise stated, is my original work and that I have not previously (in its entirety or in part) submitted it for grading in this module/assignment or another module/assignment.*

# Abstract

Microfluidic devices, or lab-on-a-chip technologies, are designed to simulate certain laboratory processes where functionality such as transporting, merging, splitting and mixing of fluids are necessary. The devices are also designed for functional autonomy and ease of use to allow an operator with no laboratory experience to perform experiments under the supervision of a professional who is familiar with the device. The size, weight and potential autonomy of these devices, combined with their ability to be programmed to perform a particular task of analysis, could bring medical diagnostics to rural areas, where the infrastructure development of a laboratory is not possible.

Microfluidic devices are already used in various industries. However, the light actuated digital microfluidic (LADM) model has yet to be developed for commercial use. The device differs from the industry standard in terms of how the fluid droplets are actuated. The new design model holds potential advantages, such as reducing manufacturing costs and significantly increasing processing speed, as well as expanding the array of possible device functions.

This project investigates the possibility of using polymers as functional layers of the LADM device. During the project, the material properties of two polymers are tested for their suitability as a photoconductive layer and a hydrophobic layer in LADM devices. The project also identifies the mathematical correlation between the varying process parameters in the deposition process of a hydrophobic fluoropolymer to the contact angle and the deposition rate of the polymer. These results directly contribute to the growing body of research on polymer based microfluidics.

A literature study contextualises the history of microfluidics and the various microfluidic platforms. A more detailed view of LADM devices and the increasing role of polymers in microfluidics lays the platform for the experimental chapters. A series of experiments are conducted to identify critical material properties and performance characteristics of the polymer materials. The observations and conclusions are discussed and recommendations for future work are proposed.

The experimental research on the polymer materials was conducted at the state-of-the-art Fraunhofer ENAS institute under supervision of the divisional head, Dr. Jörg Nestler. The instrumentation and optical setup used for the photoresistance measurements were calibrated by the laboratory technicians. The hardware and software used for the measurement of the droplet contact angle is manufactured by the industry leading supplier. The methods and results of the studies were verified by the Fraunhofer ENAS technicians.

The polymer P(VdF- HFP) is found to be a suitable dual layer (dielectric and hydrophobic) of a LADM device. Contact angles of water droplets ranged between 98°and 104°indicating its hydrophobicity, complementing its dielectric properties shown in the literature.

The polymer P3HT:PCBM is exposed to light (580nm and white light) for short periods of time. The resistance measured through the layer at the illuminated area responded within 0.5s of light exposure, as well as to the removal of the light source. The minimum resistance measured was 64MΩ. Continuous and prolonged light exposure resulted in a reduced resistance long after the light source was removed.

19 Si-wafers coated with a fluoropolymer, in a process varying input parameters, were measured for their thickness and contact angle. Two equations are obtained from a regression analysis which yields the contact angle and deposition rate of the fluoropolymer based on the variable input parameters of the deposition process.

# Contents

# List of Figures

*List of Figures* viii

# List of Tables

# Nomenclature

**Variables and functions**

| | |
|---|---|
| $\theta$ | static contact angles with applied voltage. |
| $\theta_0$ | static contact angles without applied voltage. |
| $\epsilon_r$ | relative permittivity of the dielectric. |
| $\epsilon_0$ | permittivity of free space. |
| $V$ | applied voltage. |
| $\gamma$ | liquid/filler media surface tension. |
| $d$ | dielectric thickness. |
| $\epsilon_{ri,liquid}$ | relative permittivity for the liquid. |
| $V_{i,liquid}$ | voltage drop for the liquid |
| $\epsilon_{ri,filler}$ | relative permittivity for the filler |
| $V_{i,filler}$ | voltage drop for the filler. |
| $d_i$ | thickness of layer $i$. |
| $i$ | each of the layers (dielectric, top-and-bottom hydrophobic, and liquid/filler) |
| $(f)$ | frequency. |
| $f_c$ | critical frequency. |
| $P_r$ | pressure of deposition process (mTorr) |
| $P_o$ | power Bias of deposition process (W) |
| $G_{C4F8}$ | $C_4F_8$ flow rate (sccm) |
| $G_{CHF3}$ | $CHF_3$ flow rate (sccm) |

## Acronyms and abbreviations

| | |
|---|---|
| LADM | light actuated digital microfluidic |
| ENAS | Electronic Nano Systems |
| IAP | Institute for Applied Polymer |
| P3HT:PCBM | poly(3-hexylthiophene) : [6,6]- phenyl-C61-butyric acid methyl ester |
| P(VdF-HFP) | poly(vinylidene fluoride-co-hexafluoropropene) |
| DSA | Drop Shape Analyzer |
| EWOD | electrowetting on dielectric |
| GPC | gas-phase chromatography |
| HPLC | high pressure liquid chromatography |
| CE | capillary electrophoresis |
| MEMS | microelectromechanical systems |
| PDMS | poly(dimethylsiloxane) |
| LADs | linear actuated devices |
| PCR | polymerase chain reaction |
| MALDI-MS | matrix assisted laser deportation/ionization mass spectrometry |
| DMF | digital microfluidic |
| UV | ultra violet |
| ITO | indium tin oxide |
| PTFE | polytetrafluoroethylene |
| FEP | fluorinated ethylene propylene |
| PFA | perfluoroalkoxy |
| PC | polycarbonate |
| COC | cyclic olefin copolymer |
| CVD | chemical vapour deposition |
| PECVD | plasma enhanced chemical vapour deposition |
| IC | integrated circuit |
| PFA | perfluoroalkoxy |
| OPV | organic photovoltaic |
| BHJ | bulk heterojunction |
| CL | chemiluminescence |
| DSA | Drop shape analysis |
| sccm | standard cubic centimetres per minute |

# Chapter 1

# Introduction

## 1.1. Background

At the time of writing it is reported that there are over 17 000 publications on microfluidics - also known as "lab-on-a-chip" technology [1]. In these publications there are solutions for a myriad of different problems that might occur. However, the successful development of a working microfluidic device remains a risky venture. Quite often the various existing functional layers or devices are not compatible to, or combinable with each other. In addition, many of the methods used to fabricate these materials and devices are too expensive, especially for rural locations [2]. The use of organic polymers to design a microfluidic device in a bottom-up design approach might provide the answer to some of the aforementioned problems. A device is necessary that accommodates a wide range of unit operations, that can be manufactured at low cost and high volume, that can perform assays that serve a functional purpose and which is designed for commercial success.

Microfluidic devices, or lab-on-a-chip technologies, are designed to simulate certain laboratory processes where functionality such as transporting, merging, splitting and mixing of fluids are necessary. These devices range in size between 2 $cm^2$ and 30 $cm^2$ and manipulate droplets of nano- and microlitre volumes. Economies of scale advantages have made this platform fortuitous for industries where specific fluids and chemical reagents are scarce and expensive. The devices are also designed for functional autonomy and ease of use to allow an operator with no laboratory experience to perform experiments under the supervision of a professional who is familiar with the device.

As the word "chip" indicates, the devices are designed to digitally communicate the experimental results directly to a computer, further decreasing the potential error of human involvement and data documentation. The size, weight and potential autonomy of these devices, combined with their ability to be programmed to perform a particular task of analysis, could bring medical diagnostics to rural areas, where the infrastructure development of a laboratory is not possible. Microfluidic devices are already used in various industries, but a light actuated digital microfluidic (LADM) model has yet to be

developed for commercial use. The device differs from the industry standard in terms of how the fluid droplets are actuated. The new design model holds potential advantages, such as reducing manufacturing costs and significantly increasing processing speed, as well as expanding the array of possible device functions.

The advancement of microfluidic research is especially important to a country such as South Africa, where the integrated use of lab-on-a-chip technology can bring significant relief to rural communities where there is a lack of medical assistance and point-of-care diagnostic facilities.

## 1.2. Problem statement

Ideally, a cost effective and fully functional LADM device should be able to be constructed from polymers. From the wide range of polymer materials available, a selection has to be made where the material properties can fulfil the necessary function of the various layers of this device. If this can be achieved, these devices could be manufactured at lower costs, both for small scale and large scale production, enabling both the academic and commercial industries.

If this cannot be achieved, the conventional methods of constructing such devices from glass and metallic materials will delay their development and limit their applications and distribution. The fabrication equipment for making polymer devices are cheaper [3] than those required for making semiconductor infrastructures, such as wet benches or reactive-ion etching facilities [4]. This inherent reduction in overhead costs will enable a much wider research effort towards the optimisation of polymer based microfluidics.

This project investigates the possibility of using polymers as functional layers of the LADM device. During the project, two previously unused materials were tested and yielded promising results in their use as part of a LADM device.

The use polymers as the functional layers of the LADM device provides unique research to the field of microfluidics. Apart from considerations over cost and availability, the stack-layer nature of the device necessitates careful selection of materials based on their physical characteristics, ease of manufacturing and toxicity. Most importantly the compatibility with the other layers, both in the assembly and functioning of the device, must be considered, because each layer of the device performs an individual task as well as a unified task in conjunction with its bordering layers. To address the problem of synthesizing a polymer based LADM device, various experiments are performed to establish the use of polymers as functional layers in a LADM device.

## 1.3. Methodology

This study involves the analysis of material samples received from Fraunhofer IAP and Fraunhofer ENAS. The sample set of 5 (M15, M17, M18, M19, M20) from Fraunhofer IAP each consisted of a layer stack of ITO covered glass, P3HT:PCBM and P(VdF-HFP). Two of these samples (M18 & M20), were used to conduct tests on the photoconductive polymer layer of P3HT:PCBM, to establish various material properties necessary for the successful functioning of such a layer in a LADM device. In total, four experiments are performed to investigate these material properties.

Samples M15, M17 & M19 are used to test the hydrophobic behaviour of the polymer P(VdF-HFP). To test this, the surface contact angle of $1\mu l$ droplets were measured. By using a Krüss Drop Shape Analyzer (DSA100) and its accompanying software, it was possible to accurately dose, photograph and measure the contact angle of $\mu l$ volume droplets.

Fraunhofer ENAS supplied 19 silicon wafers that were subjected to a fluoropolymer deposition process where the process parameters were varied during the fabrication process. These samples were tested for their material thickness by Fraunhofer ENAS personnel through an ellipsometry test. Additionally, 740 measurements of the contact angle of $\mu l$ de-ionised droplets on the 19 Si-wafers were measured. The results of the ellipsometry tests and contact angle tests were then related to the process parameters of the deposition process of the fluoropolymer through a regression analysis. Two formulas are obtained from this analysis that predicts the deposition rate and the observed contact angle.

## 1.4. Chapter summary

In Chapter 2, the history of microfluidics is first addressed to lay a foundation of understanding in the functioning and application of these devices. Next, the different microfluidic platforms are defined and discussed with more specific focus on the pressure driven- and electrokinetic platforms. In the discussion of electrokinetic platforms, the concept of Electrowetting on Dielectric (EWOD) is first discussed, which is the principle on which the LADM device is based upon.

Next the chapter turns its focus to illustrate how the modelling of EWOD devices can be done using theoretical mathematical models. The review then moves to the LADM device in more detail, with specific focus on the different layers and their function in the device. Lastly the use of polymers in microfluidics is explored, with a focus both on the fabrication methods of some polymer microfluidic devices. There is also an

introduction of fluoropolymers, as well as the polymers (P3HT:PCBM) and P(VdF-HFP), which are all discussed further in the experimental chapters to follow.

In Chapter 3, the polymer (P3HT:PCBM) is tested for its suitability as a photoconductive layer in a LADM device. Four experiments aim to establish different physical characteristics of the material. The observations and conclusions of the experiments are discussed along with recommendations for future tests on P3HT:PCBM or similar materials.

In Chapter 4, tests are done on the polymer Poly(vinylidene fluoride-co-hexafluoropropene) P(VdF-HFP). The initial purpose of the polymer layer was to be the dielectric layer of the LADM device. However, this chapter investigates its suitability as a dual layer. As a dual layer, in addition to having a high dielectric constant, the material should also display hydrophobic properties. An experimental section documents the results of a contact angle measurement test. The observations and conclusions of the experiments are discussed along with recommendations for future tests on P(VdF-HFP) or similar materials.

In Chapter 5, 19 Silicon wafers are deposited with a fluoropolymer in a process that has 5 variable process parameters. After cutting the wafers in to two identical halves, the one half is subjected to a ellipsometry test, to determine the material thickness, which by factoring in the deposition time, yields the deposition rate (nm/s). The other half of the wafers are used to conduct contact angle measurements of $1\mu l$ de-ionised water droplets.

The aim of this chapter is then to establish a mathematical correlation between the varying process parameters in the deposition process, to the contact angle and the deposition rate. Two equations are obtained through the means of a regression analysis.

# Chapter 2

# Literature Review

## 2.1. Microfluidics History

Microfluidics is a technology field which has developed due to the advances made primarily in four different fields: molecular analysis, biodefence, molecular biology and microelectronics [5]. The advances made in gas-phase chromatography (GPC), high-pressure liquid chromatography (HPLC) and capillary electrophoresis (CE) revolutionised chemical analysis. These techniques were focused on the analysis of chemicals and molecules in a capillary format. The advancement of the laser in optical detection, in addition to the aforementioned advances in molecular analysis technologies, made it possible to simultaneously achieve results, using small volumetric samples, that had both high resolution and high sensitivity. These advancements in micro-analytical methods encouraged development of new, more compact and -versatile formats for them, and to investigate other applications of micro-scale methods in chemistry and biochemistry [5].

The rapid rise of genomics in the 1980s presented another platform where microfluidic research and application could provide answers to new problems of the industry. Once DNA sequencing was gaining momentum, the microanalysis of molecular biology required analytical methods that again needed results with high throughput, and higher sensitivity and resolution than had previously been contemplated in biology. The field of Microfluidics offered to overcome these new problems with new approaches. [5]

Biodefence, defensive measures taken to protect against an attack using biological weapons, presented a very different motivation for the advancement of microfluidics [5]. In the 1990s the end of the cold war brought support from the US Department of Defence for programmes aimed at developing field-deployable microfluidic systems that were designed to serve as detectors for chemical and biological threats. The financial stimulus brought about from these programmes resulted in the rapid growth of academic microfluidic technology.

The fourth, and most important contribution to the development of microfluidics

was microelectronics. Initially, the hope was that the success of silicon microelectronics and that of microelectromechanical systems (MEMS), would be directly applicable to microfluidics. Although initial designs did use silicon and glass, the disadvantages soon became apparent. In biological analyses, where the use of light is necessary, opaque and expensive silicon proved to be a hindrance [5]. The focus soon shifted to find a working material that was optically transparent and a soft elastomer. The properties of poly(dimethylsiloxane), or PDMS, were entirely distinct from silicon and much more suited for microfluidic use. However, the mechanical, thermal and chemical stability of silicon, steel and glass have meant that microelectronic technologies have remained indispensable for the development of microfluidics and have served as materials with which to build specialized systems.

The last two decades of research has tried to emulate the functionality of microelectronic devices. Integrated circuits contain many individual units that each perform a different and verifiable task. The whole device can only achieve its specified task when all the units operate together in a predictable and consistent manner.

In microfluidics these units perform the operations necessary for fluid handling. The typical unit operations in a microfluidic device are fluid transport, -mixing, -valving, -metering, separation, incubation, reagent storage and release, as well as incubation [6]. The physical units that perform these operations are microvalves, micropumps, micromixers and other micro liquid handling parts. The greatest challenge for the future of microfluidics, and especially the successful commercialization thereof, will be to integrate the various parts into a microfluidic platform that is designed for a specific task, which could combine various unit operations.

## 2.2. Microfluidic Platforms

Daniel Mark defines a microfluidic platform as follows: "A microfluidic platform provides a set of fluidic unit operations, which are designed for easy combination within a well-defined fabrication technology. A microfluidic platform paves a generic and consistent way for miniaturization, integration, automation, and parallelization of (bio-)chemical processes" [6].

Microfluidic platforms are subdivided into 5 groups, according to their dominating main liquid propulsion principle. These 5 groups are capillary, pressure driven, centrifugal, electrokinetic and acoustic [6]. Within these groups all current microfluidic platforms can be categorised, as can be seen in Figure 2.1.
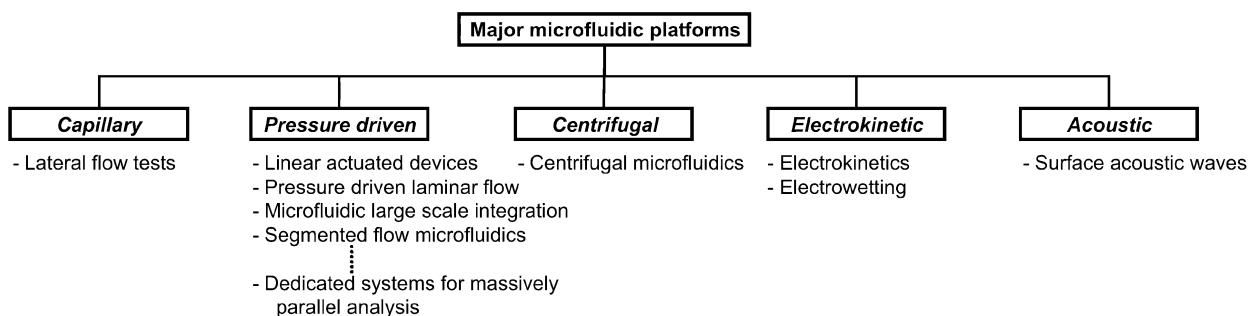
**Figure 2.1:** Microfluidic platforms (according to [6])

In this review, the focus will be only on pressure driven and electrokinetic platforms. Most microfluidic devices currently in use fall under the *pressure driven* category, so it will serve as the industry standard to compare the new Electrokinetic platforms to. Within the pressure driven category, the linear actuated devices and pressure driven laminar flow devices will be reviewed. The electrowetting platform will be reviewed in more detail in the electrokinetic category, with a specific focus on the light-actuated digital microfluidic device or LADM.

The rest of Section 2.2 will follow a similar structure when introducing a new microfluidic platform. Firstly, the platform is characterized and the main principle is presented first. Following that, the platform's unit operations or functions, as well as their typical applications are briefly discussed. Lastly, an overview of the strengths and limitations of each platform is given.

## 2.2.1. Pressure driven microfluidic platforms

### Lateral flow tests

In terms of droplet actuation methods, lateral flow test devices are the most basic type of microfluidic platforms. Through capillary forces alone,the liquids are controlled or manoeuvred by the hydrophobicity and feature size of the microstructures that the substrate is made of. All of the required chemical reagents, needed to perform the test, are pre-stored. The test results are typically identified optically. With different molecules presenting as a colour change [6, 7].

The standard device layout and functionality can be seen in Figure 2.2. The main parts of the device consists of an inlet port and a result detection window (Figure 2.2(a)). The core of the device is made up of different wettable materials, as well as all the necessary biochemicals to perform the test. The capillary capacity is strong enough to

wick the sample through the whole length of the device [7].

Practically the fluid sample, a droplet of $\mu$l capacity, is dropped onto the inlet into a sample pad (Figure 2.2(b)). This closed design greatly contributes to sterility by holding back contaminates and dust. Once inside the device, the micro structures allows for the capillary forces to transport the fluid into the conjugate pad. There, the first type (of three) antibodies conjugate onto a signal-generating particle and are rehydrated before binding to the antigens in the sample (Figure 2.2(c)). The binding of antigens and antibodies continue as the sample moves through to the detection pad [6,7].

The tests typically have a control line and a test line. Here, different antibodies help to reveal relevant information. On the test line (Figure 2.2(d)), a second type of antibody couples with the particles in the fluid that are coated with antigens and thus show the presence or absence of a specific analyte. On the control line, a third type of antibody couples with particles which did not bind to an analyte. The presence of these particles indicate a successfully processed test. Results are typically obtained after 2 to 15 minutes [6,7].
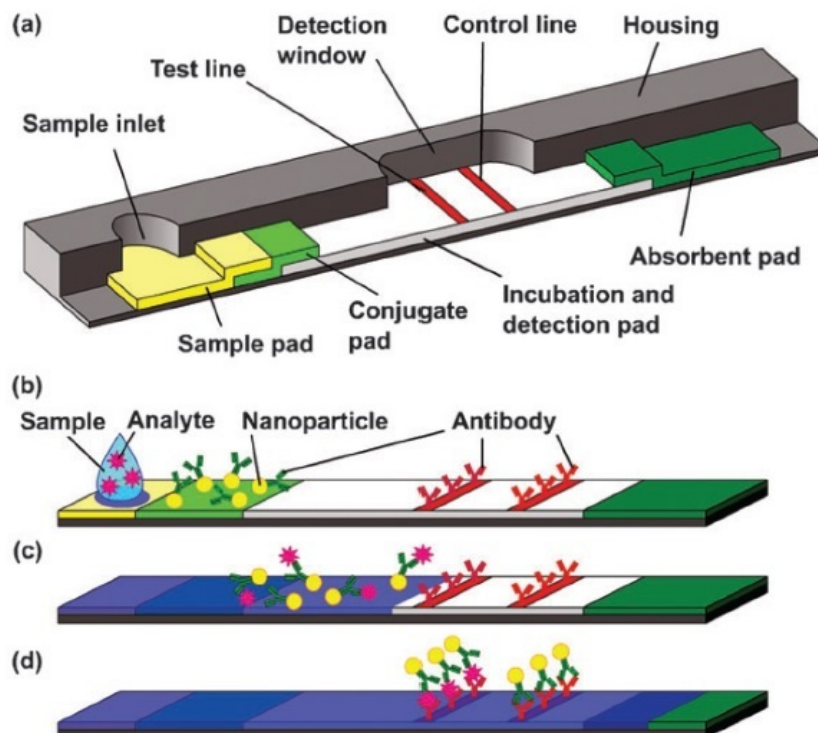


**Figure 2.2:** Functionality of lateral flow tests [7]

There is an odd relationship between the commercial success of lateral flow devices and the scarcity of publicised material on the devices. These devices outperform most other

microfluidic devices in terms of simplicity, cost, robustness, handling, and the number of implemented lab-on-a-chip applications, yet there are only a handful of noteworthy papers on their materials and construction. One may wonder if there are many company secrets that are kept unpublished [7].

**Linear actuated devices**

Compared to lateral flow devices, linear actuated devices perform better in quantification of results and could have more applications. These devices are also more complex as a processing device and disposable test carrier [6]. The actuation of the fluids in linear actuated devices (LADs) is mostly in a linear one dimensional flow path with no branching. The actuation force is created by means of mechanical displacement of flexible pouches or plungers [6]. Each device can perform multiple tests by virtue of having disposable test carriers and portable result analysers. Typically results are obtained in this sample-to-result process within a couple of minutes and in some cases, up to an hour [6].

LADs make use mainly of two unit operations: liquid transport, by means of mechanical displacement and reagent pre-storage in the disposable test carrier [6]. Both liquid and dry reagents, as well as fluids, are pre-stored in disposable cartridges. The fluids are moved in linear channels with no inter-branching, although a third unit operation, mixing, can be implemented by displacing fluids between adjacent reservoirs [8]. Mixing can also be achieved through atomic forces by making use of weak bonds between a channel and an adjacent reservoir.

The first device of this kind the i-Stat used different disposable cartridges for analysing a myriad of blood parameters using the same hand held analyser for both sample processing and result readout [9]. By making use of pre-stored calibration solutions, point-of-care results, that have good agreement when compared to laboratory tests, can be obtained within 2-6 minutes [10, 11].

The flexible inputs and operating conditions of LADs makes them ideal for point-of-care applications. These include the handling of fluid samples ranging from $10 - 100\mu l$, processing times of less than an hour, the ability to pre-store reagents and a high degree of assays, provided by the various disposable cartridges [6]. However, there is a small price to pay for this flexibility, which is an unchangeable imprinted protocol specific to a singular test. The devices are also limited to few unit operations, which hinders the implementation of more complex assays, such as integrated genotyping with a plurality of genetic markers or multi-parameter assay.

**Pressure driven laminar flow devices**

The liquid transport mechanism pressure driven laminar flow platforms is based on pressure gradients within the channels in which the fluid is actuated. Over a wide range of flow rates, hydrodynamically stable laminar flow profiles are achieved inside the microchannels. These laminar flows are also achieved over a wide range of flow rates. A range of actuation methods are used such as external or internal pressure sources that make use of syringes, pumps or micropumps. Other methods include gas expansion principles and pneumatic displacement of membranes. To process the samples and reagents, they are injected into the chip inlets. This is done either batch-wise, or in a continuous mode [6].

The unit operation of mixing is the most important of the pressure driven laminar flow devices. In this process, the laminar flow streams of at least two liquids are mixed through controlled diffusion at a microfluidic channel junction [12]. Laminar flow can also be applied to achieve flow focusing. In this instance a central and two symmetric side channels are connected at a junction forming a common outlet channel. Variation in the flow rates of these channels result in the accurate adjustment of the lateral width of the central streamline within the common outlet channel. By focussing the flow in this manner, micro-objects are suspended in the liquid flowing through the central channel. This well aligned and defined streamline position is advantageous in isolating the micro objects suspended in the solution [12, 13], as is shown in Figure 2.3.
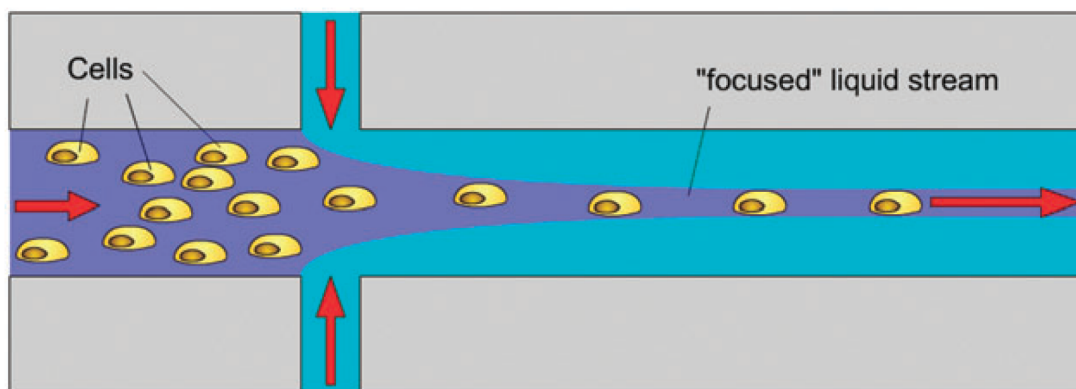


**Figure 2.3:** Focussed flow of micro-objects (according to [12])

These micro objects are typically living cells or micro-droplets of a liquid stream. These micro objects can then be separated or sorted from the main liquid stream [6]. This is achieved through some force acting selectively on the suspended micro-objects, while the liquid stream stays more or less unaffected. Geometrical barriers, magnetic forces, acoustic principles or hydrodynamic principles are responsible for these actions of separation.

The use of microvalves can play an important part in the functioning of pressure driven

laminar flow platforms by controlling flow rates. However, no standard methods or designs have emerged that have easily achieved these microvalves. Thus the implementation of valves remain difficult on this platform [14, 15].

A novel application of these devices is through a technology called PTM or phase transfer magnetophoresis. Magnetic microparticles are attracted with the use of off-chip rotating permanent magnets. This attraction enables the microparticles to be transferred between adjacent streams. This method has applications in DNA purification, DNA-extraction and free-flow magnetophoresis [6, 16, 17]. Nucleic acid diagnostics have been a constant source of research and many publications have documented microfluidically automated components based on pressure driven laminar flow chips [15, 18]. One such device can bee seen in Figure 2.4. However, integrating the complete system remains a challenge because of how challenging the inclusion of sample preparation is [18]. The time required for these type of tests such as DNA purification [6], polymerase chain reaction (PCR) tests, electrophoretic separation- and detection of pathogens, is now less than 30 minutes [19]. An example of such a device is shown in Figure 2.4, where only the sample analysis step was not integrated in the microfluidic chip.
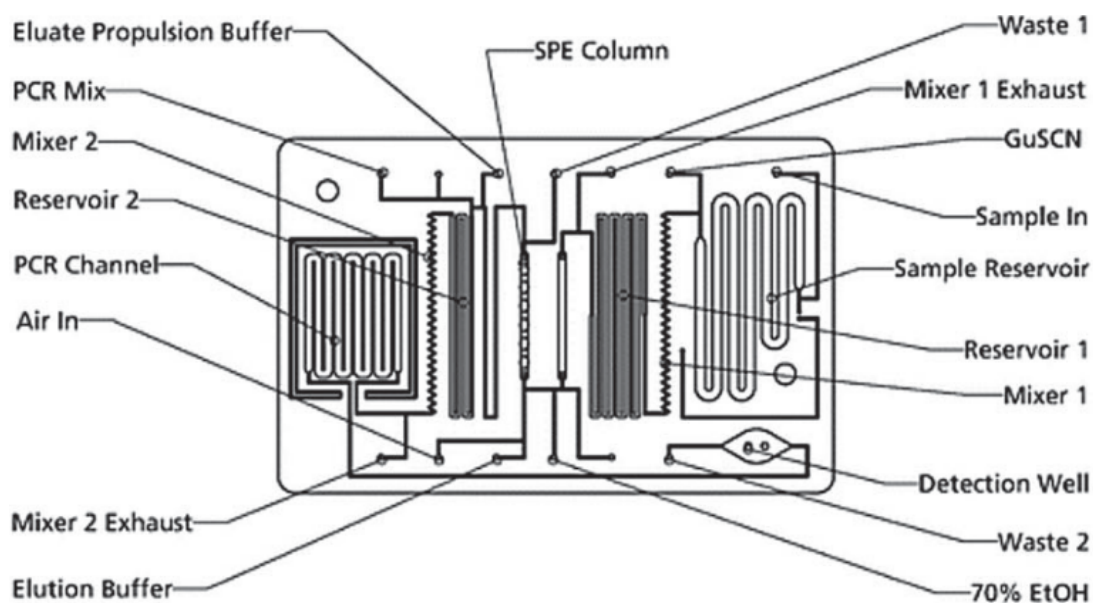


**Figure 2.4:** Pressure driven laminar flow device for batch-wise nucleic acid diagnostics (according to [6])

The biggest strength of the platform lies in its potential for continuous processing of samples [6] in what is referred to as batch-wise tests. Future applications will make increased use of online monitoring, for which continuous processing and monitoring are of the utmost importance. Due its functionality, these platforms could be constructed with polymer mass-production technologies, such as injection moulding, enabling inexpensive

disposable microfluidic chips. This is discussed in more detail in Section 2.5.

The design of this devices necessitates having the pressure source separate from the disposable chip. This adds further manual steps of operation and decreases its portability. The phenomenon of Taylor dispersion of streamwise dispersed samples hinders the accurate tracking of analyte concentrations on the platform [20]. The platform is designed and optimised for mixing and separation unit operations, but limited in other operations.

### 2.2.2. Electrokinetic microfluidic platforms

**Electrowetting devices**

Electrowetting platforms are specifically designed to actuate droplets rather than flow streams [21]. The droplets are often immersed within another fluid (either liquid or gas) to protect the droplet from factors such as evaporation and contamination. Droplets are created through various means. Making use of a water-in-oil emulsion or air-liquid combinations, droplets are formed and can then be actuated through the device [22]. The droplets are moved across a hydrophobic surface to maximize manoeuvrability and control. This can also be achieved by making use of a surface that is coated with a fluorinated oil [23]. A two-dimensional array of individually addressable electrodes are structured in another layer adjacent to the hydrophobic layer [24]. The voltage difference between the electrode and the droplet governs the droplet's behaviour. Thus the unit operations of the device is programmable and crucially, reprogrammable to perform different tasks [25].

Although the principle of electrowetting was demonstrated by Lippmann as early as 1875 [26], it was not until the 1990's that it became a feasible principle to use in practice. The introduction of the dielectric layer between the electrode and the hydrophobic layer, made it possible to increase the applied voltage by several orders of magnitude whilst avoiding electrolysis of the fluid [26]. As seen in Figure 2.5, the applied voltage creates a build up of charge in the dielectric layer. The ions in the fluid rearrange to congregate near the opposite polarity. The larger the applied voltage, the larger the charge build up in the dielectric layer, and thus the contact surface of the droplet enlarges to try and equalize the charge on the surface [26].
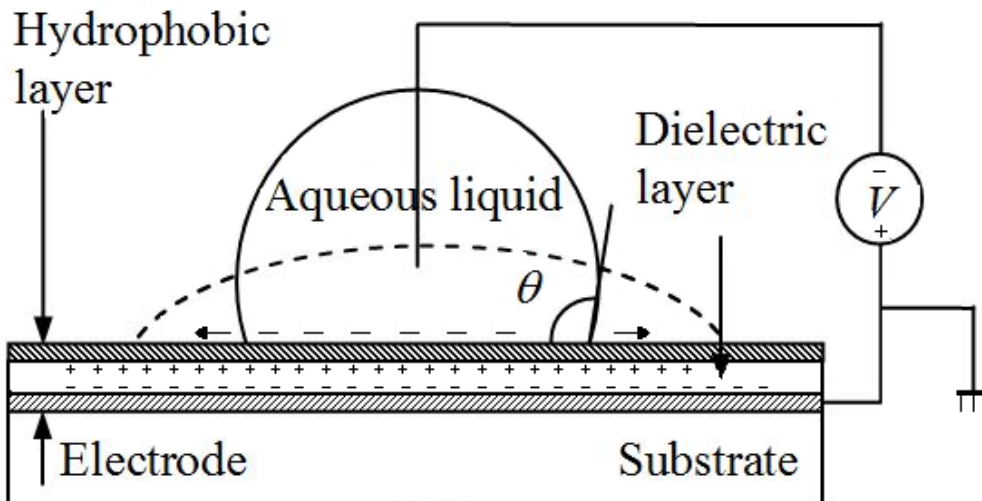
**Figure 2.5:** Electrowetting on dielectric principle

This effect, called Electrowetting on Dielectric (EWOD) [27], is used as a method to actuate the droplet over the hydrophobic surface. The principle succeeds due to the surface tension of the fluid, holding the droplet together in a spherical shape. As a new adjacent electrode is activated, the corresponding area of the dielectric layer becomes electrically charged. If the newly charged area makes partial, overlapping contact with the droplet, then the wetting behaviour causes the edge of the droplet to spread out over the newly charged area [28].

Through this process, the droplet is manoeuvred by the electrode array on one side and by a large planar ground electrode on the opposite side (see Figure 2.6). The surface tension of the droplet *drags* the whole droplet together, thus completing the movement of the entire droplet from the area over one electrode to another [29]. If the aim is to move the droplet in a line, adjacent electrodes that form the path the droplet must take are activated and deactivated moving the droplet along. This flexibility in the movement is programmable and thus enables the implementation of different assays on the same device.
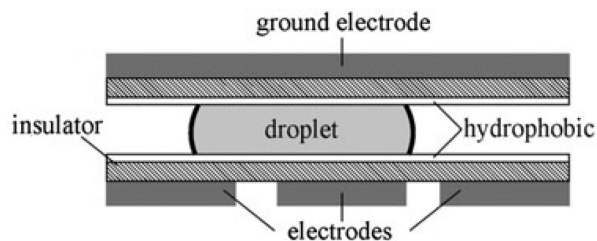


**Figure 2.6:** Electrowetting on dielectric with ground electrode

Droplet formation, is the fundamental unit operation of EWOD devices. Droplets are

extruded from an on-chip reservoir by activating a series of electrodes near the edge of the reservoir [30]. Droplets as small as 20nl can be metered with a standard deviation of 2% [30]. The same principle can be applied to a single drop, in order to split it in two [25]. The actuation of the droplets is achieved using the EWOD effect, which can also be used to merge two droplets together. By moving merged droplets back and forth between at least two electrodes, the droplet content can be mixed [31].

Living organisms and cells can be housed inside the droplets of an EWOD device. Multiple biological assays can be programmed and performed as well as diagnostic tests on biological fluids. These processes are most commonly limited by either biofouling, loss of biomolecules or surface pollution. The use of silicon oil has been demonstrated to reduce biofouling. [23]

Droplet actuation provides a much better platform for biological experiments over single phase continuous flow systems, mostly due to its flexibility of application and reusability on the same hardware.

Various fluids have been demonstrated to work on EWOD devices [32], [30]. These include:

- Aqueous solutions

- Organic solvents

- Ionic liquids

- Aqueous surfactant solutions

- Biological fluids

  - Blood, plasma, saliva, serum, urine, sweat & tears

In the field, various different applications of EWOD based devices have been documented. The successful demonstration of colorimetric, enzymatic assays on various bio fluids as well as glucose concentration measurements on biofluids including, serum, plasma, urine and saliva are documented [30]. These demonstrations indicate the broad spectrum of health indicators that can be tested by such devices. The automation of sample preparations of peptides and proteins for matrix assisted laser deportation/ionization mass spectrometry (MALDI-MS) is also possible on EWOD platforms [33]. Also, a PCR assay has been conducted on a EWOD platform by putting a droplet (at rest) through a temperature cycling process [34].

Sample manipulation with EWOD has many advantages compared with other microfluidic mechanisms, such as precise droplet actuation, less contamination risk, minimal dead volume, efficient reagent mixing, short reaction time, simple chip fabrication, and flexibility for integration.

Furthermore, EWOD brings significant advantages to the system development, such as low-cost chip fabrication, simple system construction, low energy consumption, and system portability [6, 30, 34].

Disadvantages of EWOD devices include the evaporation of working fluid, although the use of oil reduces this risk. In cases where the dielectric material is too thin, or porous in structure, electrolysis can occur if the applied voltage is too high. The stability of hydrophobic layers can decrease over time, decreasing the reusability of a device [6].

## 2.3. Theoretical Modelling of EWOD devices

This sections aims to create a realistic model of a polymer-based LADM based on an electromechanical framework. Earlier models have aimed to estimate the forces acting on a droplet in a DMF device, based on the EWOD principle.

Forces that affect droplet movement can be divided into driving and resistive forces. Early attempts of estimating the driving forces were based on a thermodynamic approach using the Young-Lippman equation [35], [36]

$$\cos(\theta) = \cos(\theta_0) + \frac{\epsilon_0 \epsilon_r V^2}{2\gamma d} \tag{2.1}$$

where $\theta$ and $\theta_0$ are the static contact angles with and without applied voltage, respectively, $\epsilon_r$ is the relative permittivity of the dielectric, $\epsilon_0$ is the permittivity of free space, $V$ is the applied voltage, $\gamma$ is the liquid/filler media surface tension, and $d$ is the dielectric thickness. The Young-Lippman model predicts droplet motion based on the capillary pressure that results from asymmetric contact across the droplet. However, this model fails to account for liquid-dielectrophoretic forces and thus another model will be used [35].

In order to relate the intrinsic properties of the individual layers to the forces acting on the droplet, and thus the functionality of the completed LADM device more accurately, a mathematical model of the device will be set up. This model will aim to represent the driving and resistive forces acting on the droplet through an equivalent circuit of the system. The capacitive and resistive properties of each layer are influenced by the material properties, their geometry and also by both the working- and filler fluid used in the device [35].

Earlier circuit-models of digital EWOD devices (using physical electrodes) are based on an electromechanical framework. These models estimate the amount of energy, $E$, capacitively stored in the system as a function of frequency and droplet position along the axis of droplet propagation (from the inactive to the active electrode) [24]. The model assumes that the cross-sectional area of the drop can be approximated as a square with sides of length $L$ (see Figure 2.7).
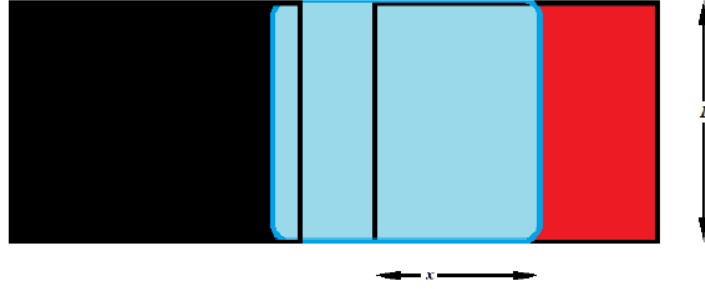


**Figure 2.7:** Top view of adjacent electrodes (black and red) with overlapping droplet (blue) with sides of length L [24]

The energy is expressed as

$$E(f,x) = \frac{L}{2}\left(x\sum_{i=0}^{n}\frac{\epsilon_0\epsilon_{ri,liquid}V_{i,liquid}^2(j2\pi f)}{d_i} + (L-x)\sum_{i=0}^{n}\frac{\epsilon_0\epsilon_{ri,filler}V_{i,filler}^2(j2\pi f)}{d_i}\right) \quad (2.2)$$

with $\epsilon_{ri,liquid}, V_{i,liquid}$ and $\epsilon_{ri,filler}, V_{i,filler}$ are the relative permittivity and voltage drop for the liquid and filler fluid portions of the electrode, respectively, and $d_i$ is the thickness of layer $i$. The subscript $i$ refers to each of the layers (dielectric, top-and-bottom hydrophobic, and liquid/filler).

The change in energy as $x$ goes from 0 to $L$ is equivalent to the work done on the system, therefore, differentiating (2.2) with respect to $x$ yields the driving force as a function of frequency ($f$):

$$E(f) = \frac{\delta E(f,x)}{\delta x} = \frac{L}{2}\left(\sum_{i=0}^{n}\frac{\epsilon_0\epsilon_{ri,liquid}V_{i,liquid}^2(j2\pi f)}{d_i} - \sum_{i=0}^{n}\frac{\epsilon_0\epsilon_{ri,filler}V_{i,filler}^2(j2\pi f)}{d_i}\right) \quad (2.3)$$

For each combination of layer-stack materials, their geometries and the liquid combinations, there is a critical frequency, $f_c$. In this model, the force acting on the droplet arises from charges accumulated near the three-phase contact line being electrostatically pulled toward the actuated electrode [24]. The magnitude of this force is highly dependant on the capacitive energy stored in the dielectric layer. If the frequency goes beyond that

of the critical frequency, a significant electric field gradient is established within the droplet. This will induce a liquid-dilectrophoretic force, which pulls the droplet toward the activated electrode. The force is weighted by the difference in permittivity between the liquid and filler medium [24].

There are other forces also acting on the droplet. A shear force acts between the drop and the contacting layer and a viscous drag force is acted on the droplet caused by the displacement of the filler fluid. These forces should be minimised to allow for droplet to move optimally.

## 2.4. Light Actuated Digital Microfluidic Device

The synthesis of a Light Actuated Digital Microfluidic (LADM) device is the focus of this research. The LADM device, as the name suggests, uses light as a tool to actuate droplets. The device is based on the EWOD principle (see Section 2.2.2) and retains all of the aforementioned unit operations and most of the functionality.

### 2.4.1. Optoelectrowetting

Optoelectrowetting devices differ from normal EWOD devices in the functionality of the electrodes. The physical electronic circuit layout that makes up the 2D electrode layer of the standard EWOD devices is replaced by a photoconductive layer containing virtual electrodes. Surface areas that are exposed to electromagnetic radiation (visible, UV, infrared light) become electrically conductive, and this is called photoconductivity [37].

The energy absorbed from photons raises electrons across the band gap, or excites impurities within the band gap, thus creating more free electrons and holes. This creates a flow of electrical current through the material perpendicular to the surface which is exposed to the photons. The presence of light acts as a switch to turn the virtual electrode on and off [38].

Optoelectrofluidic technologies require much less power and offer a much larger manipulation area [39]. In addition, compared to conventional electrical methods, in which fixed electrode patterns are applied, reconfigurable virtual electrodes formed by an optical manner allow parallel manipulation of a massive amount of particles at a specific region of interest over a wide area.

## 2.4.2. Functions of the layers

As seen in Figure 2.8, the device is constructed by stacking different material layers, with a gap wherein the fluid is actuated. The functionality depends exclusively on the individual material properties of each layer and the degree to which the adjacent layers correctly interact.
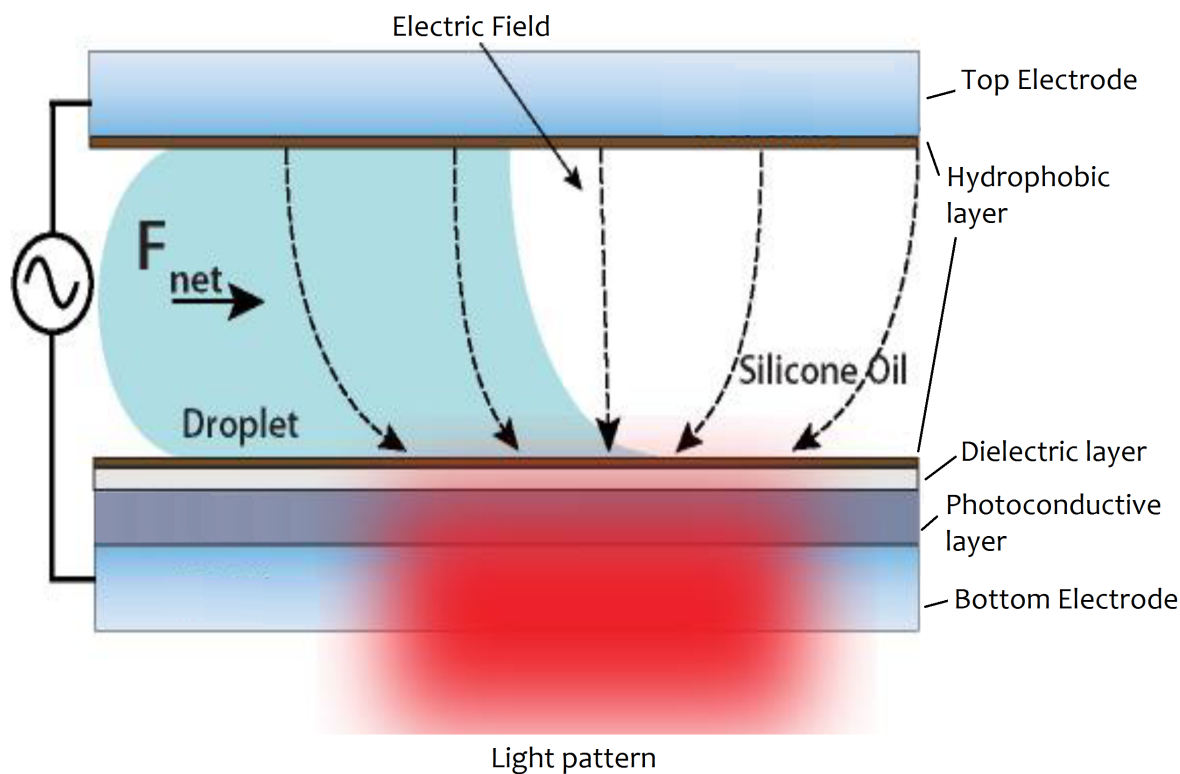


**Figure 2.8:** Light actuated digital microfluidic device [37]

**Base electrode layer**

The electrode layer is usually the first layer of the stack that is manufactured. The layer is transparent, to allow light to pass through it and contains a conductive material which is connected to the power supply.

The industry standard is an indium tin oxide (ITO) covered glass substrate. Important characteristics that have to be considered in the selection of this layer is that the material has to be able to withstand the physical and chemical effects of the manufacturing processes of the layers that are stacked on top of it.

**Photoconductive layer**

As mentioned in Section 2.4.1, the fundamental concept behind optoelectrowetting is that the conductivity of the photoconductive layer can be changed by generating excess carriers with exposure to electromagnetic radiation in the form of photons. This change reduces the voltage drop across the photoconductor and, as a result, the contact angle of the liquid droplet overlapping the illuminated region decreases. Table 2.1. summarizes the most important material characteristics necessary in a photoconductive layer in a LADM device.

**Table 2.1:** Summary of important photoconductive material properties

| Important for photoconductive material for LADM | | |
|---|---|---|
| **Low dark conductivity:** This ensures the voltage will mainly drop across the photoconductor in the absence of light. | **Visible light response:** Low cost visible light. Commercial data projectors or standard lasers can be used. | **Short carrier recombination lifetime:** This enables fast switching of contact angles and high speed actuation of liquids. |

**Dielectric layer**

The dielectric layer enables the device to be operated at a higher applied voltage while preventing electrolysis of the working fluid. A higher applied voltage translates to a larger actuation force applied to the droplet. The mathematical approximation for the the net-force on the droplet is given by

$$F_{Net} \approx \frac{\epsilon_{di}}{d_{di}} V_{di}^2 \tag{2.4}$$

where $F_{net}, \epsilon_{di}, d_{di}, V_{di}$ are the net-force per unit length, electrical permittivity of the dielectric layer material (dielectric constant), dielectric layer thickness, and voltage across the dielectric layer, respectively. From (2.4) it can be seen that a high dielectric constant and a thin layer thickness enables a higher charge to build up that can actuate the droplet more efficiently at lower power. The two main restrictions for choosing this layer, are choosing a material that can be deposited without interfering with the photoconductive or base electrode layers, and being able to withstand the voltages applied to the device. The dielectric breakdown voltage should thus be known for the thickness at which it is deposited.

**Hydrophobic layer**

The hydrophobic layer is the final layer of the layer stack to be manufactured. The main purpose of the layer is to allow for the droplet to move freely over the surface. A hydrophobic surface (see Figure 2.9) is characterized by contact angles > 90°, but preferably super hydrophobic surfaces (contact angles > 150°) are needed. As with the preceding layers, the properties of the other layers have to remain unaffected by the manufacturing process of the hydrophobic layer.
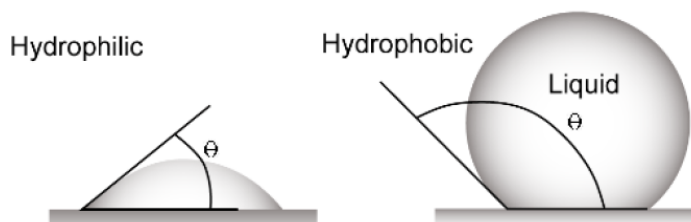


**Figure 2.9:** Contact angle of a hydrophilic and hydrophobic layer

# 2.5. Polymers in microfluidics

## 2.5.1. Background

Since their emergence in the 1970's, the use of microfluidic devices has increased tremendously due to the great potential in biomedical, point-of-care testing, and healthcare applications. The early development of microfluidic devices commonly involved silicon and glass materials as basic substrates [40].

From humble beginnings, the field of microfluidics has surged forward both in terms of research, but also in commercial application. This market-pull is mostly attributed to the success of microfluidic devices in the fields of point-of-care testing, biomedical and healthcare applications. In the early days, these devices were almost exclusively manufactured from silicon and glass materials, which was used as the basic substrates. However, since the late 1990s, the use of polymers in microfluidic devices has gained momentum due to their simple and cost effective manufacturing methods [40].

Especially when compared to devices made from silicon and glass, polymer-based devices are made from materials that are often inexpensive and that feature a wide variety of material properties. The most promising of applications thus far for polymer based microfluidic devices are disposable, biomedical microfluidics devices. However, many more fields are currently shifting their view towards polymers [4].

One of the largest advantages to the fabrication of polymer microfluidic devices are that there are no potentially hazardous etching reagents required [4]. These reagents and the equipment needed to even create prototypes are are often too expensive for researchers in low-resource settings [2]. However, polymer microfabrication has its own drawbacks, most of which are due to complexity of having multiple materials each with their own material properties that might be affected by temperature related processes. As yet, there is no one-fits-all fabrication technique for creating polymer microfluidic devices. It is therefore critical to determine polymer microfabrication strategies to ensure the successful functionality of polymer-based microfluidic devices [4].

## 2.5.2. Fabrication strategies and considerations

In recent years, analytical MEMS (microelectromechanical systems) have been fabricated in glass by means of wet chemical etching [24]. An alternative to glass-based MEMS devices are those fabricated from polymers [41]. One particular advantage to using polymers is the wide choice in microfabrication methods that can be selected to construct the device. Four of the most common microfabrication methods using polymeric materials, include spin-coating, injection moulding, hot embossing/imprinting and laser ablation. These methods are relatively inexpensive and can facilitate production in large numbers, making their use in commercial applications particularly attractive [41].

Functional material properties, such as surface charge, machinability, optical properties, molecular adsorption and others are of great importance to microfluidic applications. Material characteristics, especially those related to temperature are equally important when selecting a polymer-based substrate for both the fabrication process and the successful functioning of the device [42]. This is due to the fact that each fabrication protocol has its own unique requirements and constraints.

As an example, the thermal expansion coefficient, melt temperature and glass transition temperatures are critical in the process of injection moulding methods, as well as that of hot embossing. [42]

The thermal expansion coefficient relates to the material's dimensional change (volume or size) resulting from a specified temperature change. This parameter is important in several fabrication processes to ensure functional dimensions are maintained. It is also important when thermally bonding two or more different materials [42]. When the polymer substrate changes from a rigid, glass-like, material to a soft, but not melted, material it has reached the glass transition temperature. This is measured in terms of the stiffness

of the material (its modulus) and is dependent on its crystalline structure. The melt temperature refers to the temperature at which the polymer transitions from a solid state and starts to flow [42].

### 2.5.3. Fluoropolymers

Currently, the large majority of polymer-based microfluidic activities use the soft silicone-based elastomer polydimethylsiloxane (PDMS). These devices previously made use of glass. However, glass requires expensive fabrication facilities that uses hazardous chemicals and long processing time for fabrication. Furthermore, glass is not well suited for small detail manufacturing, like creating micro-valves [3].

PDMS has several advantages, like a high gas permittivity and high optical transmissivity. Being an elastomer, the material is easily deformed by the application of pressure. This makes it feasible for prototyping. However some drawbacks or limitations of the material are channel deformation, evaporation, sample absorption, low solvent resistivity.

Instead of trying to improve the performance of PDMS or replacing it with other materials, PDMS can be modified to compensate for its drawbacks. The surface can be modified with a hydrophobic and non-leaching material, which is also stable and has high chemical compatibility. This possibility drew the attention of research to a group of materials called fluoropolymers [3].

As early as the 1930s crystallised perfluoropolymers, such as polytetrafluoroethylene (PTFE) was discovered. This material displayed very promising properties. It is highly chemical-resistant and thermally stable. However, the material is not transparent and very hard to microfabricate. Other discoveries of semi-crystallized perfluoropolymers, such as fluorinated ethylene propylene (FEP) and perfluoroalkoxy (PFA) were made. These materials are similarly inert and stable as PTFE, but has the advantage of being transparent and melt-processable. These materials which were later to be known as Teflons were broadly used as coatings, films and additives. However, the incapability in their microfabrication, meant they could not be used for devices on micro scale for more than half a century [3].

Wood et al developed a novel method of creating a safe and cost effective way to produce a material whose properties are comparable to those of the commercial product (Teflon® AF 1601) [23]. This new method reduces the risk of contamination from solvents or surfactants.

The basic properties of fluoropolymers arise from the atomic structure of the base atoms

(carbon and fluorine) that make up the C-F bond found in all fluoropolymers, including polytetrafluoroethylene (PTFE) homopolymers [43]. The C-F bond is the main reason that fluoropolymers have many special properties that are superior to most other polymers. These special properties span across electrical, mechanical and thermal characteristics of the fluoropolymers. Additionally, these materials also have strong chemical resistance [43]. The useful material properties of fluoropolymers are [43]:

- Stability
- High continuous use temperature
- Excellent weatherability
- Excellent chemical resistance
- Excellent fire properties
- Low surface energy
- Good release properties

- Biological inertness
- Low friction
- Cryogenic properties
- Retains flexibility
- Electrical properties
- Low dielectric constant
- Low dissipation factor

By adding nanoparticles to fluoropolymers the mechanical stability, wear resistance as well as its performance after prolonged liquid exposure was improved [23]. These nanoparticles also impacted the surface roughness of the material contributing to a super hydrophobic surface [23]. Begolo et al. also used this hydrophobic fluoropolymer for temperature imaging in DMF systems due to the materials good stability and temperature sensitivity [23].

The fluoropolymer poly(tetraflouroethylene) (PTFE) was used to demonstrate very successful electrowetting results in 1996 by Vallet et al [44]. Their results showed that the low surface energies of this polymer contributed to the reduction in water droplet contact angle of 30°or more.

Fluoropolymers have also found application in other microfluidic platforms that make use of pressure driven laminar flow devices. Traditional polymers used in microfluidic platforms such as PDMS, PMMA polycarbonate (PC) and cyclic olefin copolymer (COC) cannot be used with fluorocarbon oils. Fluoropolymer microchips were made that enables the use of fluorinated oils, which is an excellent carrier oil for droplet slugs, as seen in Figure 2.10 [23].
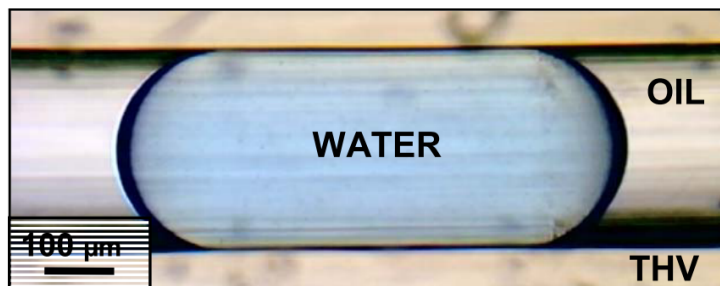
**Figure 2.10:** Micrograph of a 100nl water droplet in a $300\mu$m channel [23]

## 2.5.4. P(VDF-HFP)

As shown in Section 2.4.2, (2.4) can approximate the force acting on the droplet. According to this equation, the EWOD performance can be improved by using high-capacitance dielectric materials. To meet such requirements, extensive studies have been conducted on dielectric materials that can offer a high capacitance to lower operating voltage. Several high-$\kappa$ materials such as $Si_3N_4$, $Al_2O_3$, and $Ta_2O_5$ are typically proposed to provide a high-capacitance benefit. However, these materials need expensive and complex vacuum facilities like chemical vapour deposition (CVD), plasma enhanced chemical vapour deposition (PECVD), and sputtering for layer deposition [45].

Narasimhan et al. went further to develop and test a novel polymer based ion gel alternative. The ion gel films, which consist of a copolymer poly(vinylidene uoride-co-hexauoropropylene) [P(VDFHFP)], later discussed in Section 4, and an ionic liquid [EMIM][TFSI], 1-ethyl-3- methylimidazolium bis(triuoromethylsulfonyl)imide, was successfully fabricated through a simple spin-coating process without expensive high-vacuum facilities that are typically required for conventional IC fabrication processes [45].

Its performance as an EWOD dielectric layer is comparable to that of $Al_2O_3$ and PDMS as shown in Figure 2.11
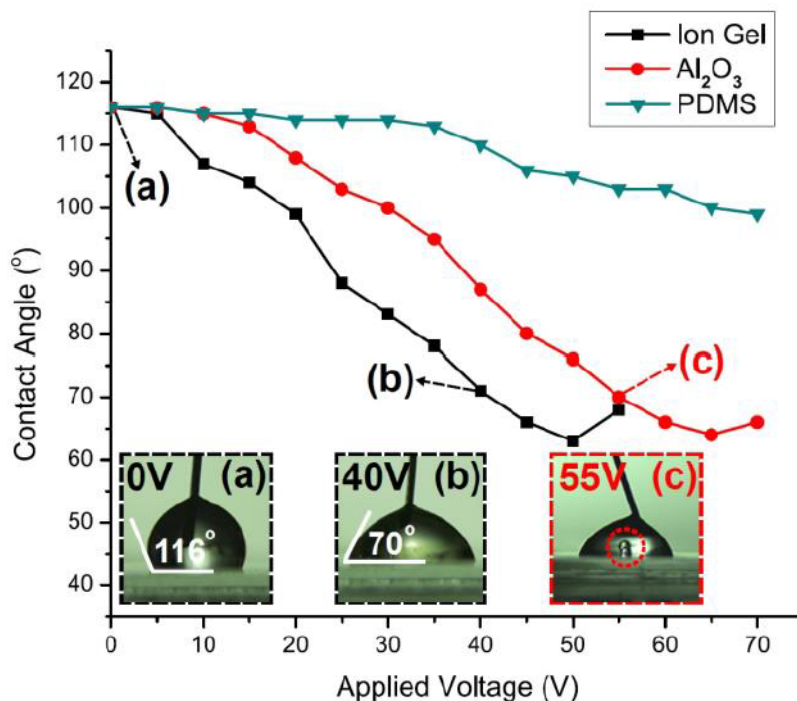
**Figure 2.11:** Comparative study of the EWOD performance of the ion gel versus $Al_2O_3$ and PDMS [45].

The ion gel is capable of lowering the operational voltage and providing an improved high-capacitance dielectric without bubble generation by electrolysis. With its relatively large capacitance and easy fabrication, the ion gel is seen as a material with great potential for 3D flexible EWOD applications.

## 2.5.5. P3HT:PCBM

### Properties and practical uses

In a conjugated polymer blend, both components can exhibit a high optical absorption coefficient and cover complementary parts of the solar spectrum [46]. In recent years the conjugated polymer regioregular poly(3-hexylthiophene) (P3HT) and [6,6]-phenyl-C61-butyric acid methyl ester (PCBM) has been used predominantly as the functional layer in organic solar cells [47], [48], [46], [49]. Organic photovoltaic (OPV) solar cells have attracted significant attention due to their great potential for large-area, light-weight, flexible, and low-cost devices [50].

The polymer has proved to be very useful as a bulk heterojunction (BHJ) [49] with the electron donor material (P3HT) and the electron acceptor material (PCBM) blended together in order to optimize both exciton separation and charge transport [51]. To date, P3HT:PCBM has shown to produce the highest device performance efficien-

cies for an organic solar cell, with efficiencies of 3-5% reported in the literature [49], [46], [47].

In addition, P3HT:PCBM has shown to display very low short-circuit dark current densities [52], which makes it a good choice for high-sensitivity detection. This particular property makes it useful as an analyte detector based on the phenomenon of chemiluminescence (CL). Xuhua Wang et al. defines CL as "the formation of a metastable reaction inter- mediate or product in an electronically excited state, which subsequently relaxes to the ground-state with the emission of a photon." [52].

In both its role as a BHJ or as a sensitive photon detection device, the performance of the P3HT:PCBM polymer is greatly influenced by its intrinsic morphology [50], which is in turn determined by the fabrication process [52], [48], [53].

**Fabrication**

By far the most common method of fabrication of a layer of P3HT:PCBM is to mix the two constituents P3HT & PCBM in a ratio of 1:(0.7 - 1) in a solution [49], [53], [52]. The solutions used in these sudies were Xylene [48], chloroform [49] and dichlorobenzene [51]. The solution is then spin-coated on to the substrate at 1000 rpm [54], before being annealed.

Throughout the available literature, it is clear that the annealing process plays the biggest part in the morphology of the crystalline structure of the polymer, which in turn influences its properties [54], [51]. There are studies that have experimented with various methods of annealing and have determined that an annealing temperature of 150°C is optimal for the efficiency of the creation of excitons and charges [47] [51]. The ideal annealing time is still uncertain, but it has been demonstrated that the majority of the effects brought on by the annealing process takes place in the first 5 seconds [53], but 30 minutes is the status quo in most studies.

The annealing process was also demonstrated by Chen et al. to red-shift the absorption spectra of the P3HT:PCBM layer, thus increasing its overlap with the solar spectrum of visible light [53]. Figure 2.12 displays this shift. In Figure 2.12(a), the three samples that were annealed (shown as red, green and blue) have moved towards the red-light spectrum compared to the black line which was only spun and not annealed. Figure 2.12(b) shows how the annealing process increases the efficiency of carrier energies within the material.
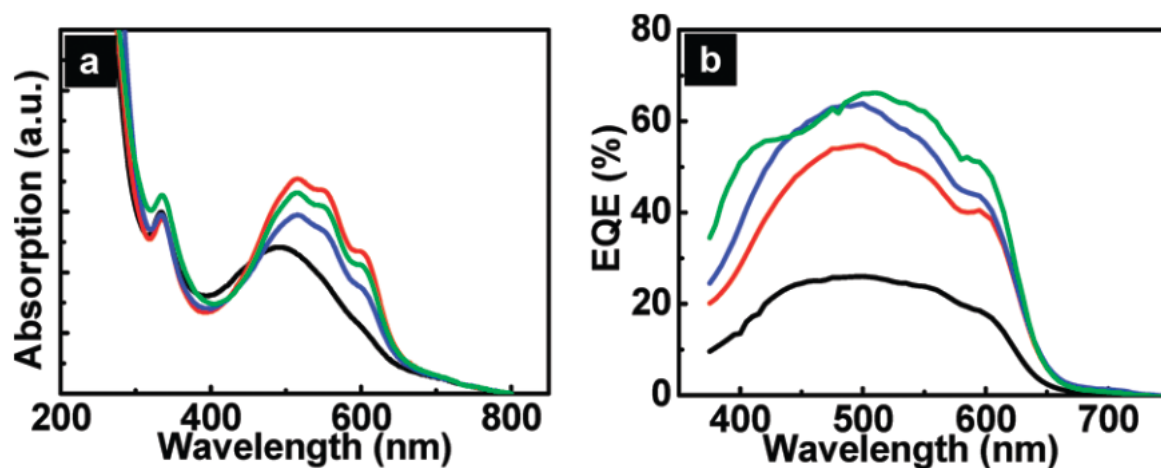
**Figure 2.12:** Ultraviolet - visible absorption and EQE of P3HT:PCBM [53]

Cugola et al. demonstrates by means of differential scanning calorimetry (DSC) the glass transition- and melting temperature for P3HT:PCBM to be 180°C and 220°C respectively [55]. Thus devices using P3HT:PCBM as a layer to which further materials must be deposited should keep annealing temperatures below 180°C.

## 2.6. Summary

The purpose of this chapter was to view the trends in microfluidics within the past forty years and see how the discovery of new materials and their properties have time and again resulted in new applications in the field of microfluidics. The process of researching new materials has thus played a crucial part in the advancement of microfluidics. Two deductions can be drawn from the research reviewed. Firstly, it is clear that over time a new microfluidic device has emerged to solve a new problem in the fields of molecular analysis, biodefence, molecular biology and microelectronics. Secondly, that polymers are playing an increasingly important role in replacing expensive materials that have complicated fabrication processes requiring tools that are not accessible in low-resource environments.

The material properties of polymers are also often found to be comparable or better to the traditionally used metals, ceramics and glasses. The ideal fabrication techniques for many of the polymer materials are still being hypothesised, though, and continues to be an area of research that is highlighting new and improved applications of these materials.

From the research, it is also clear that the field of light actuated digital microfluidics is still in its infancy. These platforms are unique in microfluidics as they require multiple materials with a varied range of material properties, all interacting towards a unit operation. The use of polymer materials for these devices have not widely been studied and many materials are yet to be documented at all.

The research provided in the following chapters aims to add to this new body of knowledge towards the use of polymers as functional layers of a light actuated digital microfluidic device.

# Chapter 3

# P3HT:PCBM as a Photoconductive layer of a LADM device

In this chapter the polymer P3HT:PCBM (poly(3-hexylthiophene): phenyl-C61-butyric acid methyl ester) is tested for its suitability as a photoconductive layer in a LADM device. Four experiments aim to establish different physical characteristics of the material. The observations and conclusions of the experiments are discussed along with recommendations for future tests on P3HT:PCBM or similar materials.

## 3.1. Function in the layer stack

As mentioned in Section 2.4.1, the fundamental concept behind optoelectrowetting is that electromagnetic radiation in the form of photons generates excess carriers inside the photoconductive layer, which then changes the conductivity of the exposed area. This change in conductivity reduces the voltage drop across the photoconductor and, as a result, there is a localised charge build up in the adjacent dielectric layer. If there is a deionised droplet overlapping the illuminated region, the contact angle of the liquid droplet decreases and effectively draws the droplet towards the illuminated region.

## 3.2. Material characteristics that influence performance

In Section 2.4.2, Table 2.1. summarizes the most important material characteristics necessary in a photoconductive layer in a LADM device.

In Section 2.5.5 the literature demonstrated that P3HT:PCBM displays the necessary properties:

1. Low dark conductivity [50], [52], [47]

2. Visible light response [54], [53], [46]

3. Short carrier recombination lifetime [47], [51], [53], [49]

# 3.3. Experiments

Five prefabricated samples were received from Fraunhofer IAP. Three of the 5 samples were a 3-layer stack comprised of a glass/ITO layer, a photoconductive layer of the material P3HT:PCBM and a dielectric layer of the material P(VDF-HFP). The other 2 samples had only the glass/ITO layer and the photoconductive layer, P3HT:PCBM. For purposes of investigating the photoconductive properties of the material, only sample M18 and M20 will be used, since the experimental procedure relies on measuring the resistance on the actual photoconductive layer. The extra layer of P(VDF-HFP) on the other 3 samples means that it is not possible to determine the photoconductive properties directly from measurement. Table 3.1 shows a summary of the sample properties.

**Table 3.1:** Potsdam sample summary

| Sample | Substrate | Layer 1 | Layer 1 thickness (nm) | Layer 2 | Layer 2 thickness (nm) |
|--------|-----------|----------|-------------------------|----------|-------------------------|
| M15 | Glass/ITO | P3HT:PCBM | 1100-1200 | P(VDF-HFP) | 300-350 |
| M17 | Glass/ITO | P3HT:PCBM | 800-900 | P(VDF-HFP) | 40-121 |
| M18 | Glass/ITO | P3HT:PCBM | 800-900 | | |
| M19 | Glass/ITO | P3HT:PCBM | 920-960 | P(VDF-HFP) | 100-150 |
| M20 | Glass/ITO | P3HT:PCBM | 920-960 | | |

These experiments aimed to investigate the properties of a photoconductive polymer, P3HT:PCBM, to establish whether it could serve as a possible candidate for LADM devices. A total of 4 different experiments were performed, each designed to investigate different material properties. A summary of these experiments and the material characteristics they investigated can be seen in Table 3.2.

**Table 3.2:** Experiments on photoconductive layer

| Experiment | Material Property Investigated |
|------------|--------------------------------|
| Photoresistance test | Visible light response |
| AC Voltage tests with LCR meter | Visible light response ; Dark conductivity |
| Spectrometer test | Optimal light frequency response |
| Laser experiments | Dark conductivity ; Carrier recombination lifetime |

## 3.3.1. Experiment 1 - Photoresistance measurement

**Experimental setup and method**

The initial experiment aimed to establish whether the samples (M18 & M20) displayed photoconductive properties when exposed to light. The samples were placed above the light source of the microscope so that a focused beam with a diameter of around 2mm was projected onto the glass side of the samples.
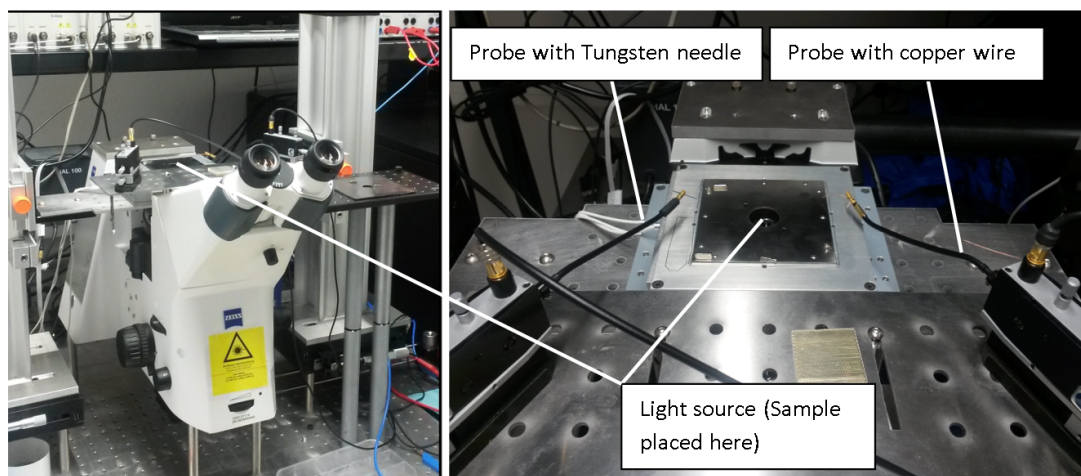


**Figure 3.1:** Optical setup. Samples M18 & M20 were placed above projected light and measured with two probes

As can be seen in Figure 3.1, two probes were used to measure the resistance of the specific area where the light was projected on. The one probe, a tungsten needle, was used to measure the ground level by scratching through the photoconductive layer and making contact with the more robust ITO layer. To test whether the needle was making contact with the ITO layer, a small corner of the sample was scratched to expose the ITO layer. A digital multimeter (Agilent 34410A) was used to test the connection between the tungsten probe and the exposed ITO layer.

The second probe was a thin and flexible copper wire, which was bent into a loop in order to not damage the surface of the photoconductive layer. The tungsten needle was placed away from the light source projection and the copper probe was placed directly in the middle of the light source projection. Five measurements were made for each sample, see Figure 3.2(a) and Figure 3.2(b).
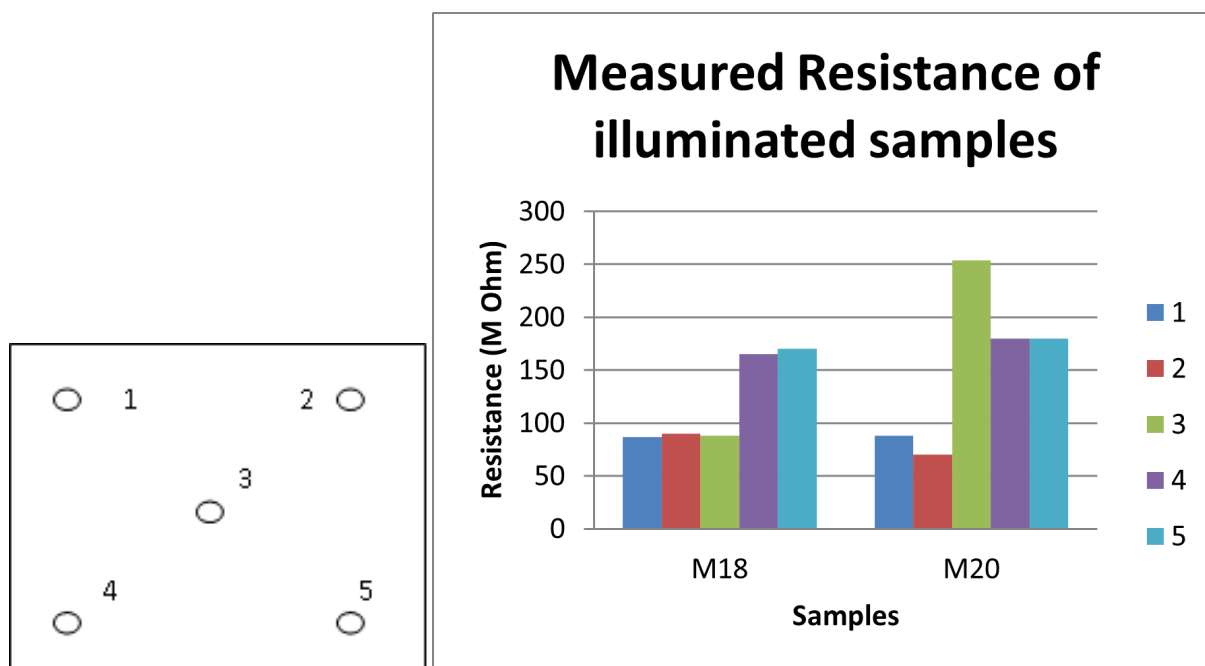
**(a)** Measurement positions on the samples



**(b)** Measured resistance for the five positions

**Figure 3.2:** Measured resistance and measuring positions for the experiments on M18 and M20

## Results

The experiments were performed in a dark room to minimize the effect of ambient light. Table 3.3 provides a summary of the average and minimum measured resistance values, as well as the factor change from maximum to minimum measured resistance. A digital multimeter (Agilent 34410A) was used to measure the resistance. The multimeter delivers a test current of 5nA for its measurements.

**Table 3.3:** Experiment 1 - results summary

| Sample | Resistance change when exposed to light | Measured Resistance | | | Light source details |
|--------|------------------|---------|---------|---------------|----------------------|
| | | Minimum | Average | Factor change | |
| **M15** | No | | | | • White light (halogen) |
| **M17** | No | | | | • Maximum intensity |
| **M18** | Yes | 87 MΩ | 119 MΩ | x17 | measured @ 0.0378 |
| **M19** | No | | | | Watt/cm² at 555 nm) |
| **M20** | Yes | 64 MΩ | 154 MΩ | x23 | |

### 3.3.2. Experiment 2 - AC Voltage tests with LCR meter

**Experimental setup and method**

Using the halogen light source and the exact experimental setup as in Experiment 1, a test was set up to determine the change in resistance compared to the size of the illuminated area. The two measuring probes were connected to a LCR meter and the device was calibrated for the circuit using a closed and open calibration. The parameters were set to 1kHz and 1.5V and the impedance was measured.

Sample M20 was tested by adjusting the focus of the light beam so that a large unfocussed beam was illuminated on the sample. Then, the focus was steadily adjusted until the smallest focused beam was illuminating the sample. The copper measuring probe was positioned in the centre of the beam throughout the test. Positions 1, 2, 3 and 5 were tested and a similar result was obtained on each position.

The hypothesis is that the illuminated area can be viewed as a rod or wire with a length, $l$ and cross sectional area, $A$. The length will correlate to the thickness of the photoconductive layer and the cross sectional area to the illuminated area. The resistance should then decrease as the illuminated area increases.

**Results**

The maximum resistance was measured when the light beam was stretched out and had the lowest flux $(W/m^2)$ and the minimum resistance was measured when the beam was fully focused and the flux was at maximum. The results were all consistent in this observation. This can be explained as while measureing at one small area of the beam, higher flux means a higher concentration of photon energy per area, which increases the current and thus reduces the resistance. A strange phenomenon was observed in each measurement: just before the beam was adjusted to its fully focused position, the resistance level greatly increased for a fraction of a second before dropping back down to the minimum resistance point when the beam reached its smallest size on the sample. A schematic representation is given in Figure 3.3.

**Schematic representation of measured resistance of M18 &
M20 over time with decreasing area of light exposure**
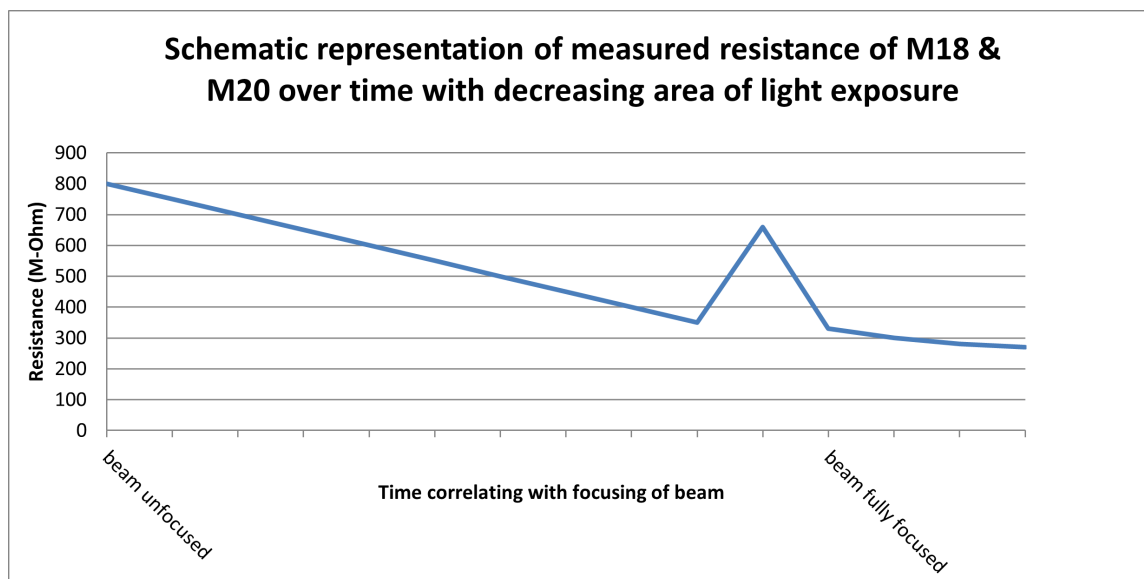


**Figure 3.3:** Measured resistance over time with linear focussing of illuminated beam

The results also identified a capacitive reactance, with the measured phase angle always negative. The values of the phase angle were not consistent and varied between -8°and -35°. From the results obtained with the LCR meter the hypothesis of the illuminated portion of the photoconductive material being seen as an equivalent rod or wire is proved false.

However, the cause of this observation lies in the measuring equipment. The contact area of the copper wire is smaller than the illuminated area, and thus the enlargement of the illuminated area only decreases the brightness of the light at the point of measurement. To properly test this hypothesis, a measuring probe has to be used that has a larger contact area than the illuminated area on the sample.

### 3.3.3. Experiment 3 - Spectrometer test

In addition to the resistance measurements, an experiment was also performed to determine at which wavelengths the samples are absorbing most light. Using a spectrometer, two tests were done, yielding two similar results that can be seen in Figure 3.4). The spectrometer measured the reflectance as a function of the wavenumber measured in $cm^-$. The results indicate very good absorption between 420nm and 590nm with the maximum absorption happening at 555nm.
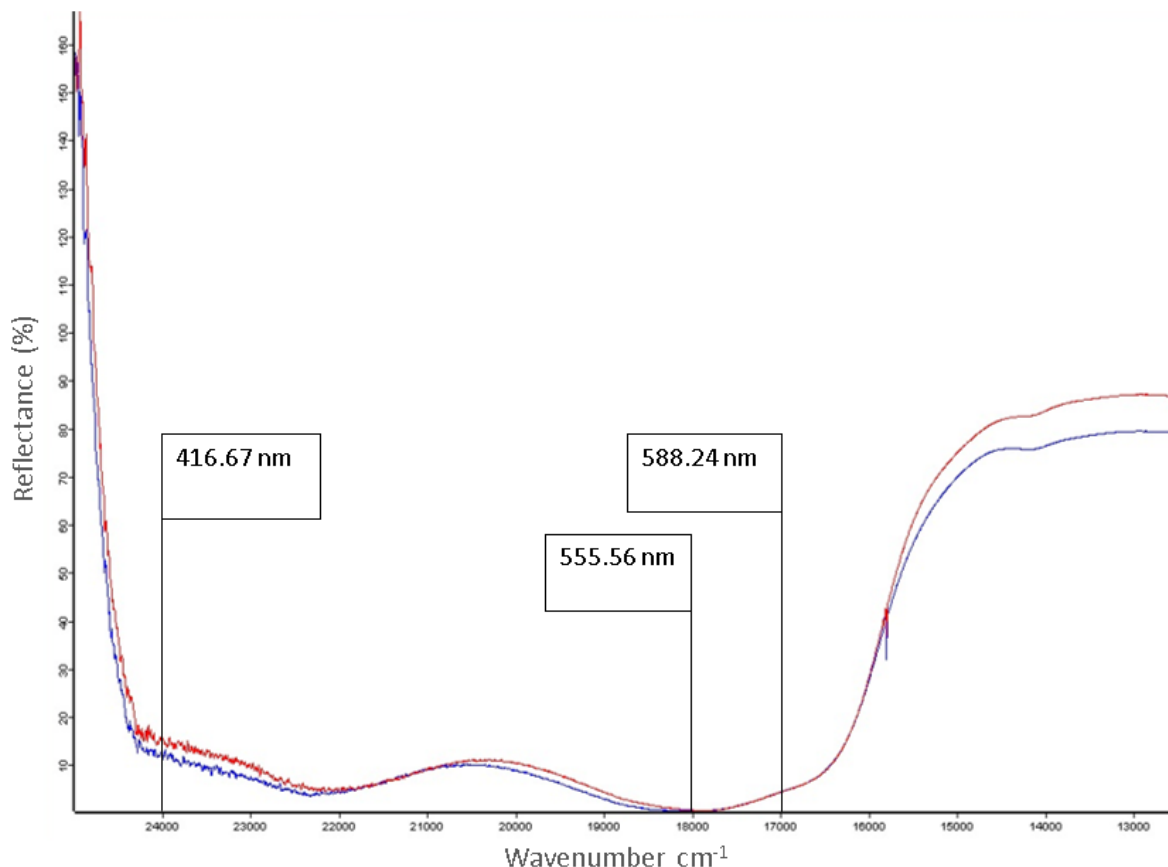
**Figure 3.4:** Spectrometer results of absorption of samples M18 (Red line) and M20 (Blue line) at various wavelengths

## 3.3.4. Experiment 4 - Laser Experiments

To further determine the photoconductive properties of the P3HT:PCBM layer in samples M18 & M20, a laser (5mW @580nm) was used to determine the drop in resistance measured at the illuminated area. The exact same setup was used as with Experiment 1. The only difference is that the light source was changed. The positional areas of Figure 3.2(a) are also referred to in this section. Three different tests were performed with the laser:

1. 48 second exposure at 50% decrements of laser power

2. Voltage sweeps at various percentages of laser power

3. Laser pulses (turning the laser on and off during measurement)

**Resistance measured over time**

Sample M18 was exposed to the laser on location number 3 for 48 seconds. The current through the sample was measured with an applied voltage of 5V. The Resistance values over time were then calculated using Ohm's Law at 100%, 50% and 0% laser power on

the same area. Ohm's law: $R = V/I$, where $R$ is resistance, $V$ is voltage and $I$ is current. Figure 3.5 shows the results.
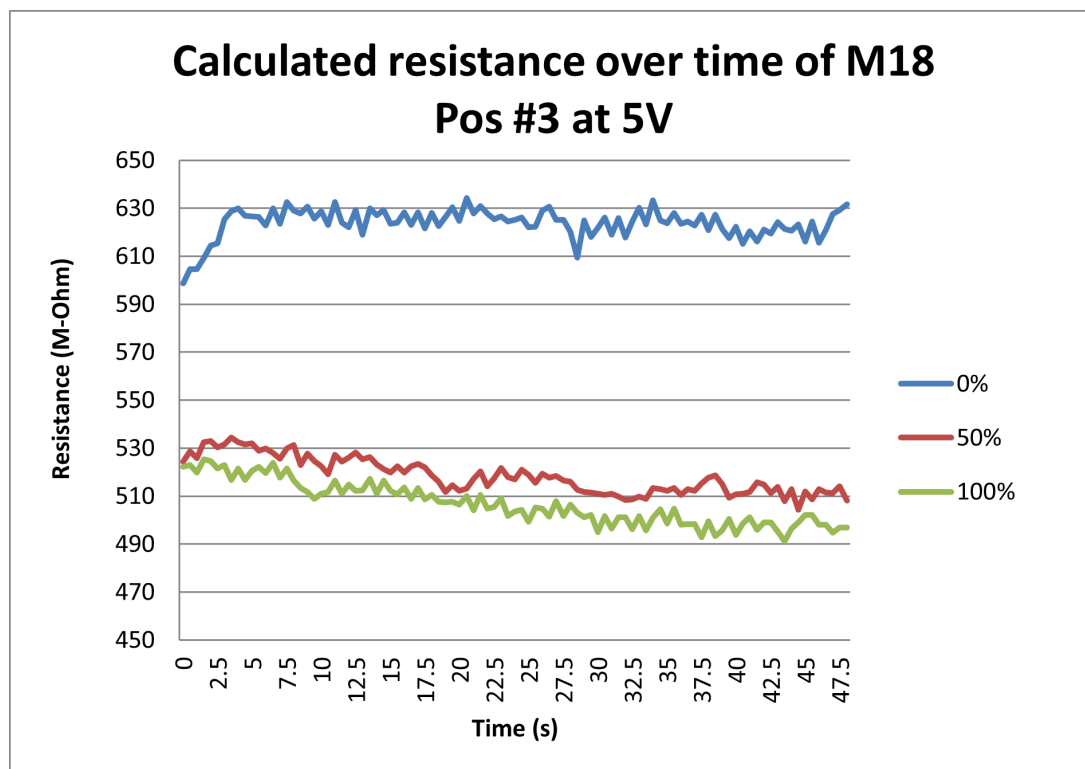


**Figure 3.5:** Calculated resistance of Sample M18 measured at location 3 over time

From Figure 3.5 it can be seen that the resistance is generally lower at maximum power than at 50% power. It can also be seen that the resistance tends to drop gradually with time. The values of the resistance measured at 0% laser power is due to the residual effects of the laser heating the sample.

Next, the measurements were made on position 2. The applied voltage was first set at 5V and two measurements were taken, indicated in brackets, to further determine the effects of prolonged light exposure. The applied voltage was then set to 10V and three measurements were made. The first measurement (10V(1)) was only measured for 31 seconds. All the measurements from Figure 3.6 were taken at 100% laser power.
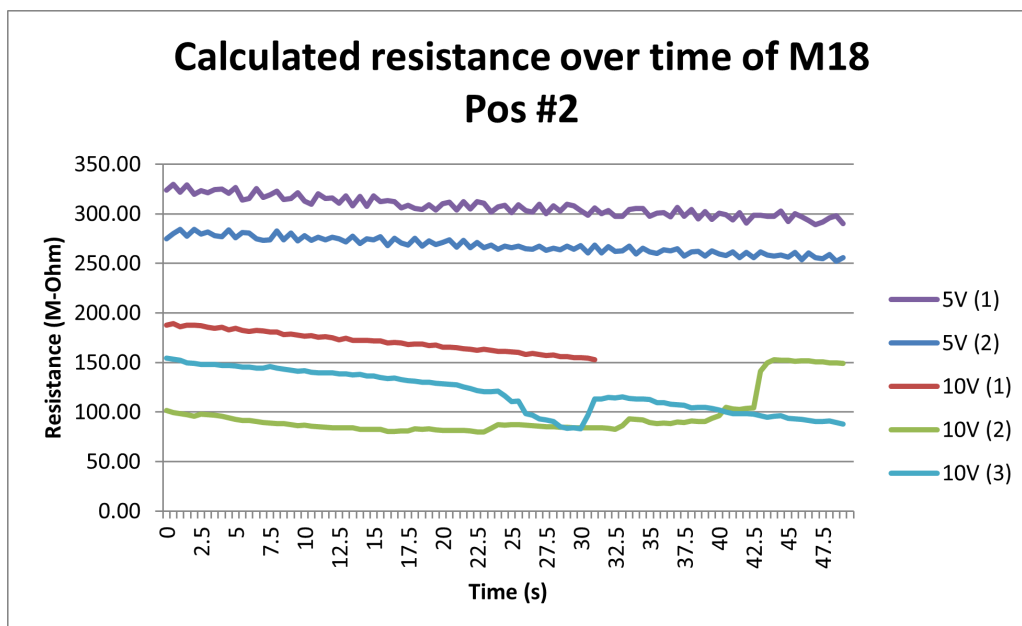
**Figure 3.6:** Resistance measured for sample M18 at 5V and 10V

From Figure 3.6 it can be seen that for the 5V measurements the variation of resistance is much more than for the 10V measurements. The measurements of 10V(2) and 10V(3) display some strange characteristics. This can be due to the measuring probes not making proper contact. In general, the trend that the longer exposure time decreases the resistance can still be found in the results. Next, Sample M20 was measured at Position 2.
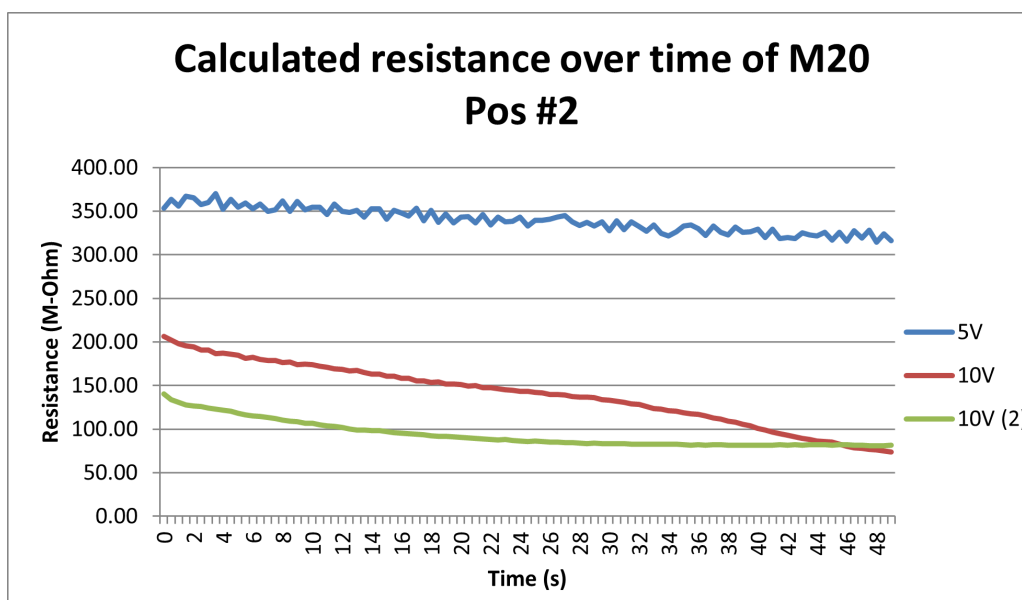


**Figure 3.7:** Resistance measured for sample M20 at 5V and 10V at 100% laser power

Similar trends were seen in the measurements of sample M20 at position 2. The lowest measured resistance (74 MΩ) was found when an applied voltage of 10V was used.

**Voltage sweeps at various laser powers**

Sample M20 was exposed to various laser power percentages on location 3. The current through the sample was measured with an applied voltage sweep from 0 to 10V. The resistance values were calculated, again using Ohm's law, and are shown in Figure 3.8 for each 20% decrement. The measurement started at 100% power and decreased to 20%.
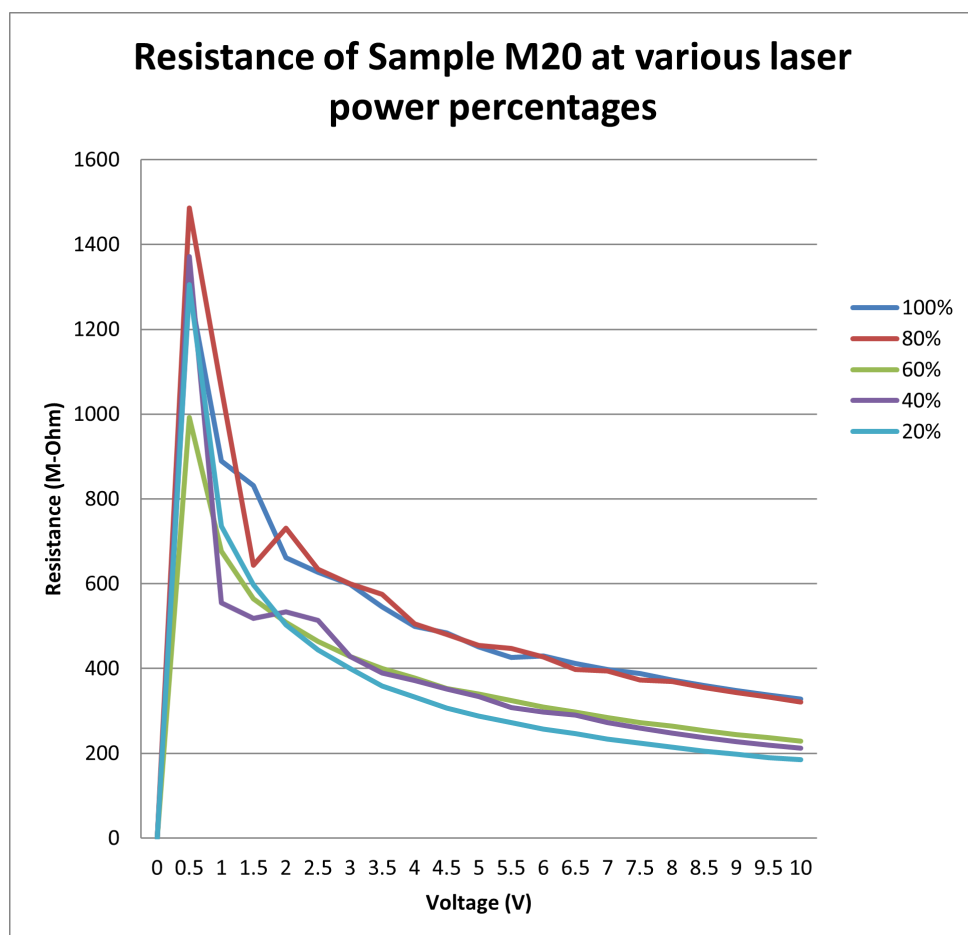


**Figure 3.8:** Resistance of sample M20 measured at position 3 through a voltage sweep from $0V$ to $10V$ at 20% incremental decreases of laser power

The general trend of the resistance declining with a higher applied voltage can clearly be seen in Figure 3.8. There is, however, a discrepancy in the data when compared to the first experiment. As the laser power was lowered the resistance dropped. This can be due to the continuous exposure of the same area being measured. The spot was illuminated for close to 14 minutes from the first measurement to the last, with the laser only briefly turned off to adjust the power. These results indicate that the carrier recombination lifetime is of sufficient time duration to still enable carrier mobilisation with a resultant current that is less determined by the light intensity and more with repeated and prolonged light exposure.

**Laser pulses**

To observe the response of the material, the resistance was calculated by measuring the current through the sample at an applied voltage. The laser was then switched on and off as indicated in the figures below. First (Blue line) the laser was set to 80% power and the laser was switched off after 10 seconds and remained off until the end of the test. The next test (Red line), the laser was initially off, then turned on after 9 seconds, and then turned off again after 40 seconds. It can be seen in Figure 3.9, that when the laser is turned on there is a significant drop in resistance when compared to when the laser was kept on for the entirety of the test.
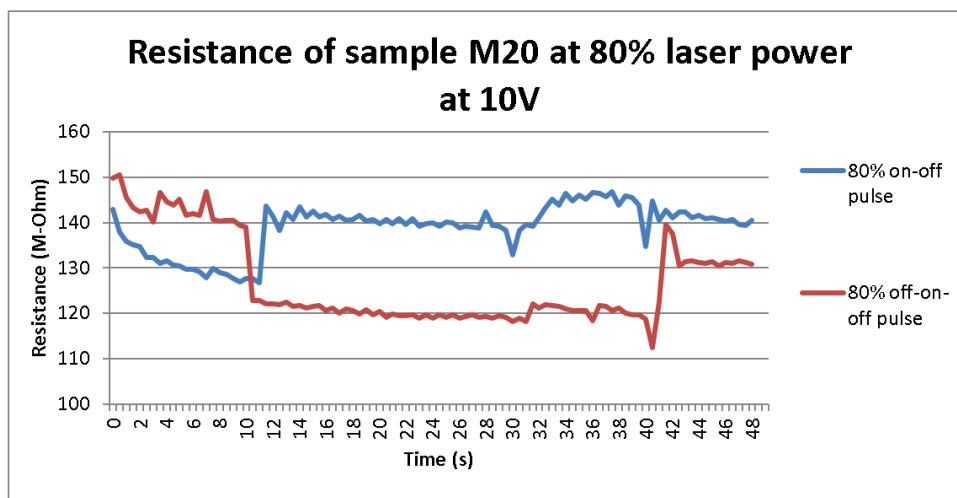


**Figure 3.9:** Resistance of Sample M20 measured at position 2 over time at 80% power with various laser pulses

For the next set of tests the laser was again set to 100% power and three similar tests were performed on the sample. Again the laser was initially off, then turned on, and then turned off again for the remainder of the test.
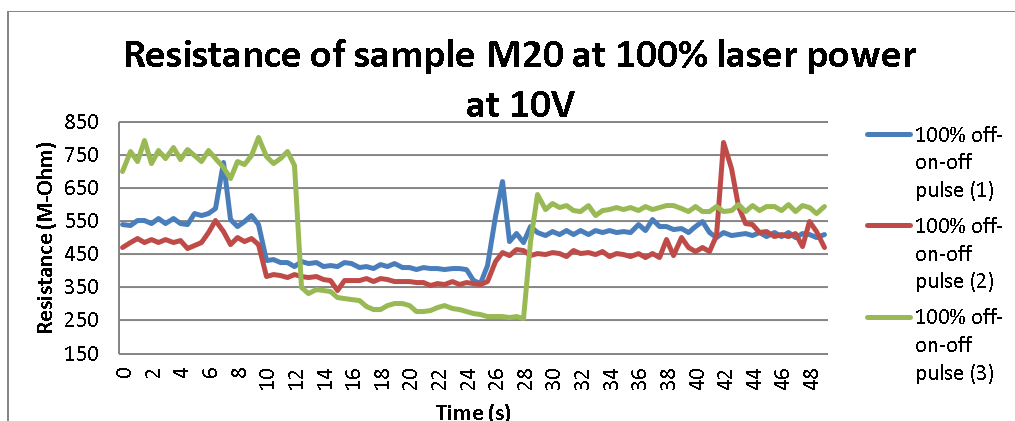


**Figure 3.10:** Resistance measured at position 2 over time at 100% laser power with off-on-off laser pulse

Figure 3.10 displays expected results. When the laser was turned on there was a drop in resistance and the resistance values were lower for each subsequent test. When the laser was turned off, the resistance increased again instantly. However, the resistance values are always lower than it was before the laser was turned on. For the final set of tests two different applied voltage values were used when measuring the resistance. The laser was initially off, then turned on, and then turned off again for the remainder of the test.
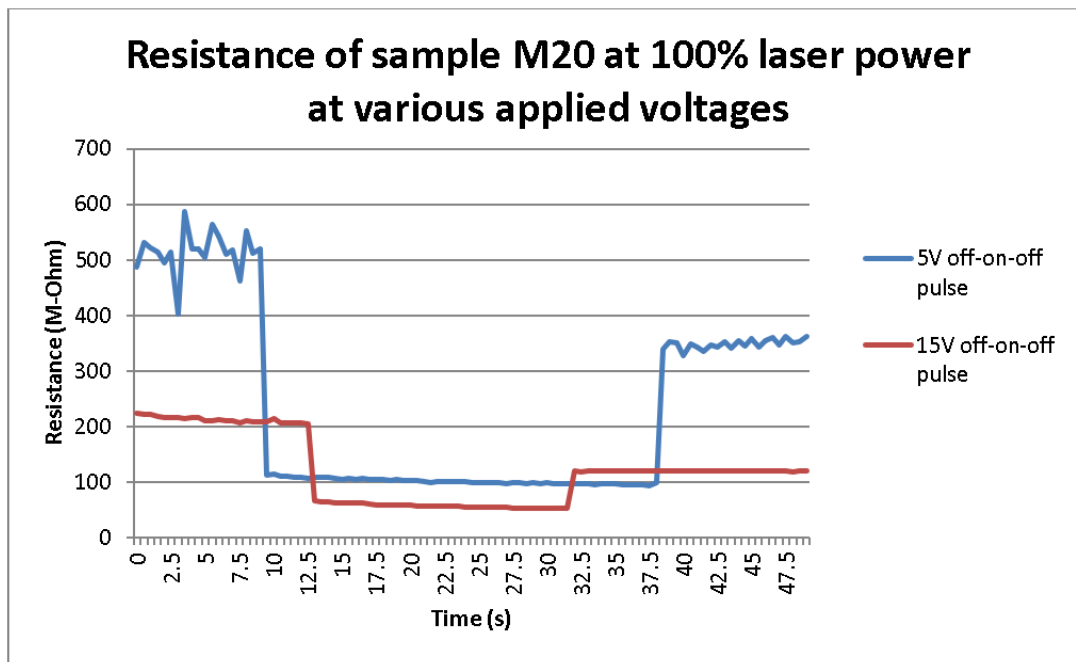


**Figure 3.11:** Resistance measured at position 3 at 100% laser power at 5V and 15V with off-on-off laser pulse

In Figure 3.11, it can be seen that there is a big difference in the resistance values, measured at 5V and 15V, when the laser is initially off. The difference is much smaller when the laser is turned on. It was seen that at an applied voltage of 50V, the area where the probes were measuring was destroyed, but the areas around the spot remained in working condition.

## 3.4. Observations and conclusions

### 3.4.1. Experiment 1 - Photoresistance measurement

The photoresistance test was set up to determine whether there is a response, measured as a reduced resistance through the photoconductive layer, due to the application of light in the visible spectrum. A halogen light with a full white-light spectrum and maximum intensity of $37.8\text{mW/cm}^2$ at a wavelength of 555nm was used for the test. The tests were performed in a dark room and measurements were taken with a digital multimeter that delivers a test current of 5nA when measuring.

There were a few observations that were made during the analysis of the results:

- The resistance-drop is strongest in the centre of the illuminated area and decreases to zero (drop in measured resistance) outside of the illuminated area.

- The maximum measured resistance ($1.5\text{G}\Omega$) was a device limit of the digital multimeter (Agilent 34410A).

- Once the light source is removed, residual resistance remains for an amount of time that is related to the intensity, as well as the duration of the previous exposure.

- The photoconductance varied over the area of the samples.

The two measured samples, M18 and M20 showed a minimum resistance of $87\text{M}\Omega$ and $64\text{M}\Omega$ respectively. With these observations it can be argued that the material P3HT:PCBM does display a electric response to visible light. The observation of a prolonged effect of the photon energy from the light source, after it has been removed is indicative of the carrier recombination lifetime. The variance of the measurements over the five positions of the sample (Figure 3.2(a)) is likely related to the variance in material thickness or crystal morphology, which in turn could be related to the annealing time and temperature of the sample.

### 3.4.2. Experiment 2 - AC Voltage tests with LCR meter

The same experimental setup was used as in Experiment 1, but this time the measuring probes were connected to a inductance (L), capacitance (C), and resistance (R) (LCR) meter set to deliver voltage at 1.5V and 1kHz. The aim of the experiment was to test the hypothesis that the illuminated area can be viewed as a rod or wire with length, $l$ and cross sectional area, $A$. The length will correlate to the thickness of the photoconductive layer and the cross sectional area to the illuminated area. The resistance should then decrease as the illuminated area increases.

The following observations were made:

- The maximum resistance was measured when the light beam was unfocussed or at lowest flux.

- The minimum resistance was measured when the beam was fully focused or at highest flux.

- The measured resistance increased significantly just before the light beam was fully focused, upon which time it then recorded the minimum measured resistance

- With AC voltage, the measured resistance also drops over time.

- The photoconductive material displays a varying capacitance in different positions on the samples, with a negative phase angle ranging between -8°and -35°.

From these observations it can be argued that the hypothesis is proven false, but this might be due to the measuring equipment. The contact area of the copper wire is smaller than the illuminated area, and thus the enlargement of the illuminated area only decreases the brightness of the light at the point of measurement. To properly test this hypothesis, a measuring probe has to used that has a larger contact area than the illuminated area on the sample.

### 3.4.3. Experiment 3 - Spectrometer test

To establish the optimal wavelength of the light source used for these samples coated with P3HT:PCBM, the samples M18 and M20 were tested for light absorption with a spectrometer. The following observations were made:

- the samples display very good absorption throughout the visible spectrum except in the red spectrum with optimal absorption in wavelengths ranging from 416nm to 590nm.

From this test it can be concluded that white light or green/blue diodes or lasers are good light sources to use as they will defer the maximum amount of energy to the sample.

### 3.4.4. Experiment 4 - Laser experiments

To further investigate both the effect of a stronger light source in the form a of a 5mW 580nm laser, and the effect of time duration on the measured resistance, a series of three experiments were conducted. The following observations were made:

- The use of the 580nm laser did not yield a lower resistance than what was obtained with the white halogen light from the microscope.

- A continuously light-exposed are on the sample retains the effects of the light exposure (decreased resistance) for periods long after the light sourced has been removed.

- The laser pulsing indicates that the material responds rapidly (within 0.5s), both to the exposure of light and also to the removal of the light source.

- The applied voltage has a significant effect on the measured resistance - even more so than the laser power percentage, which is intrinsically linked to the current flowing through the illuminated area.

Through these observations it can be concluded that the observed minimum measured resistance is a material property, and not due to the intensity of the light source. Practically this could be of use in a LADM device, as the light source used could be a cheaper source of light like LEDs rather than high energy lasers, which has cost benefits for system costs. Furthermore, the carrier recombination lifetime and its affect of a residual drop in resistance after the light source has diminished or been removed will practically implicate longer reset times for the device between unit operations of droplet actuation.

## 3.5. Recommendations for further testing

### 3.5.1. Sample preparation

Samples should be prepared to ensure optimal performance of the P3HT:PCBM polymer layer. This procedure is discussed in section 2.5.5, but in essence the goal is to obtain a more homogeneous crystal morphology and thickness over the area of the sample. Furthermore it is recommended that a corner of the sample should be masked during the spin coating of the photoconductive layer in order to have an area of the ITO layer exposed.

### 3.5.2. Experimental recommendations

A few of the observations in the experiments discussed in Section 3.4, lays a platform for future studies and tests on the P3HT:PCBM polymer layer. Some of the recommendations are summarised here:

- A measuring probe that has a larger contact area than the illuminated area of the light on the sample should be used in order to test the hypothesis of the illuminated area functioning as a rod, with a decrease in resistance resulting from an increase in illuminated area.

- The theoretical hypothesis that photoresistance is a function of light exposure of the surrounding area, should be investigated.

- The influence of light intensity and duration of previous exposure on photoresistance measurements should be studied further and tested.

- Tests should be performed using a device that can measure resistance larger than 1.5GΩ in order to determine accurately the factor change in the resistance drop due to light exposure.

- The crystal morphology and thickness should be tested and correlated to the results obtained from the photoconductive experiments.

- The effect of heat on photoresistance measurements should be tested.

- A device which measures shorter time increments should be used to test the response time of the photoconductive material.

- Device fatigue (the increase of photoresistance of a material with increased use) should be investigated as a function of applied light power.

# Chapter 4

# P(VdF- HFP) as a Hydrophobic layer in a LADM device

In this chapter, the polymer, Poly(vinylidene fluoride-co-hexafluoropropene) P(VdF-HFP), which is the second layer of the samples M15, M17, M19 obtained from Fraunhofer IAP is analysed for its suitability as a hydrophobic layer. To analyse this, the surface contact angle of $1\mu l$ droplets were measured.

In Section 2.4.2, it was shown that P(VdF- HFP) has the appropriate properties to make it suitable as a dielectric layer in a LADM device. Due to the proximity of the dielectric layer and the hydrophobic layer, the charge that the droplet experiences is a result of the combined dielectric properties of the hydrophobic layer and the dielectric layer. Furthermore in Section 2.3 the Young-Lippman equation shows that the thickness of the dielectric material as a linear role in the force acting on the droplet. Thus, it is very beneficial to utilise a material that can potentially fulfil both the dielectric and hydrophobic roles in the LADM device.

## 4.1. Function in the layer stack

### 4.1.1. Dielectric layer

The dielectric layer enables the device to be operated at a higher applied voltage while preventing electrolysis of the working fluid. A higher applied voltage translates to a larger actuation force applied to the droplet. A high dielectric constant and a thin layer thickness enables a higher charge to build up that can actuate the droplet more efficiently at lower power.

### 4.1.2. Hydrophobic layer

The primary purpose of the layer is to allow the droplet to move freely over the surface. Furthermore, the hydrophobic surface enables the inherent surface tension in the water to pull the droplet in to a sphere. This is the *natural state* that the droplet assumes.

When the droplet experiences electrowetting from a light source illuminating the area near the droplet, the droplet is pulled down to the surface, due to the charge build-up. At that moment the droplet moves incrementally towards the focal point of the light source. As soon as the light source is removed, the hydrophobic surface again causes the droplet to assume its spherical shape. The resultant displacement is towards the previously illuminated area.

## 4.2. Measurement of droplet contact angle

In Section 3.3, the material samples from Fraunhofer IAP were described. In this section the experiment is aimed to establish the hydrophobicity of P(VdF- HFP), layer 2 of the sample layer stack. Each sample underwent the same process of measurement and the values of the measured contact angle for the left side and right side of the droplet was averaged to obtain a measurement per droplet. Sample M19 seemed to have had an anomaly in the fabrication of the P(VdF- HFP) layer, as there is an irregular distribution of hydrophobic and hydrophilic areas on the sample as can be seen in figures 4.1 and 4.2.

### 4.2.1. Experimental setup and results

Using the Krüss Drop Shape Analyzer (DSA100), it was possible to accurately dose $\mu$l volume droplets. The Experimental setup is shown in Figure 4.1.
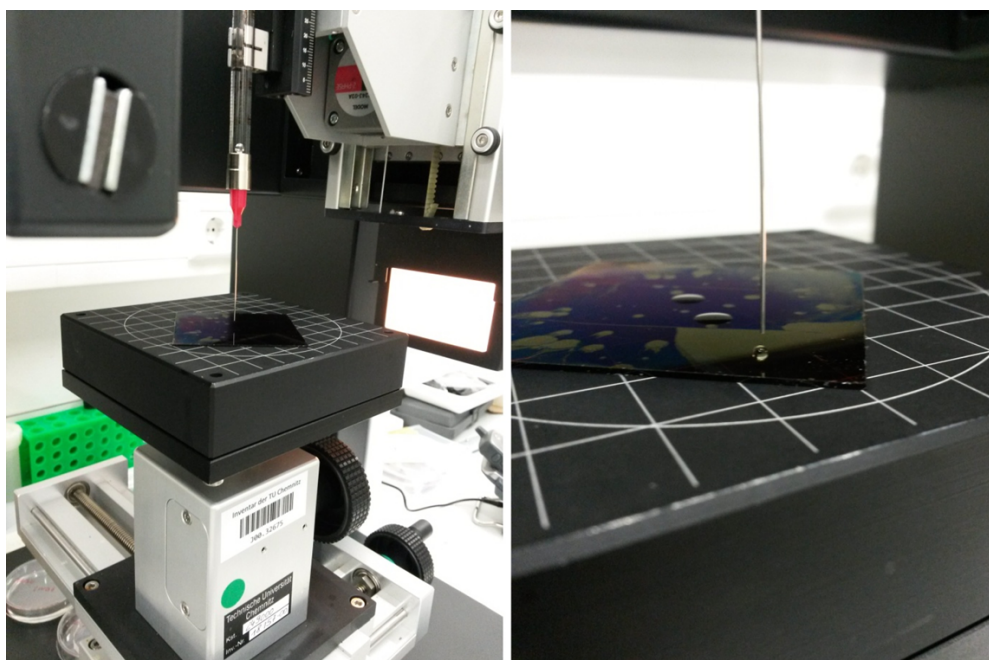


**Figure 4.1:** Experimental setup for measuring the contact angles. The image on the right shows sample M19 displaying hydrophilic and hydrophobic behaviour on various areas of the sample

**Figure 4.2:** Imaging of the $1\mu$l droplet on a hydrophilic area on sample M19

Droplets of $1\mu$l de-ionized water were discharged onto the surface of the samples. The DSA100 has a macro camera that is focused onto the droplet position and the contact angle is measure using the built in Drop shape analysis (DSA) software. In Figure 4.3 an example of one of the droplets is shown with the angle $\theta$ larger than 90°, indicating the hydrophobic contact angle.
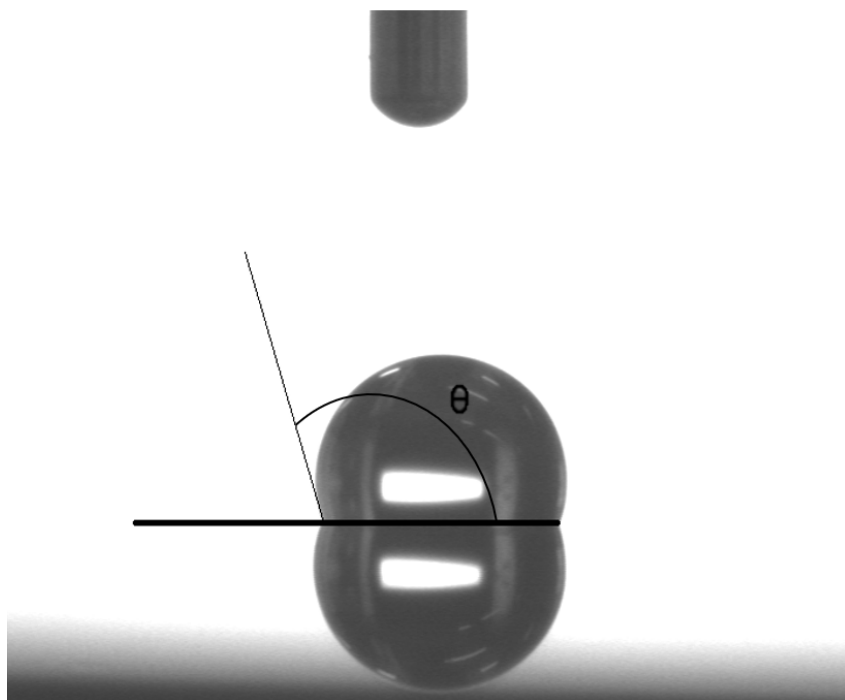


**Figure 4.3:** Imaging of the $1\mu$l droplet showing the hydrophobic contact angle

The results shown in Figure 4.4 indicate that the samples with the P(VdF- HFP) layer, except for sample M19, displayed hydrophobic effects. The average of measured contact angles for M15 and M17 were 97.7°and 103.7°respectively.
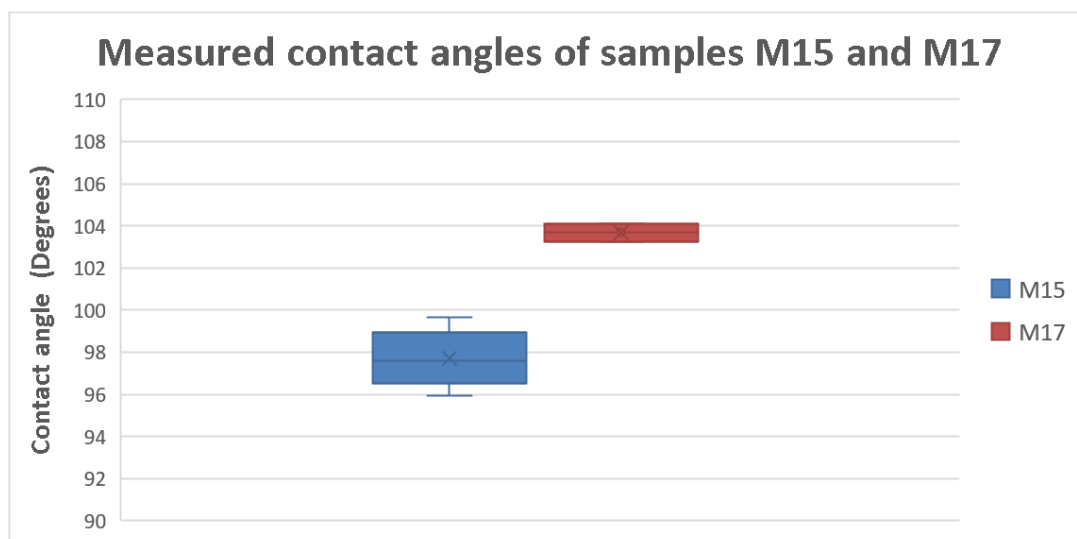


**Figure 4.4:** The measured contact angles for samples M15 and M17 showing the average of the measurements as the X and the maximum and minimum as the top and lower end of the box and whisker plot, respectively.

## 4.3. Observations and Conclusions

With the objective of testing whether the polymer layer of P(VdF- HFP) could function both as a dielectric and hydrophobic layer, the following observations were made during the experiments:

- Apart from sample M19, which displayed dramatic hydrophilic properties, all other samples coated with P(VdF- HFP) displayed hydrophobic properties with contact angles between 98°and 104°.

- Sample M19 had extreme variance over the surface of the sample in terms of the observed contact angle. It can be concluded that M19 must have experienced either a different process during fabrication or was subjected to different temperatures during annealing or transportation which caused the surface to be non-homogenous, and as a result, displayed inconsistent results when tested.

The results of obtained form testing M15 and M17, being the samples coated with P(VdF-HFP), indicate that this material could potentially fulfil the role of a dual layer, serving both as the dielectric layer and the hydrophobic layer.

## 4.4. Recommendations for further testing

Further confirmation towards the suitability of P(VdF- HFP) as a hydrophobic layer could be obtained from investigating the material structure. It is recommended to investigate the the following aspects:

- The correlation between micro-structuring / surface roughness and observed contact angles.

- The nano/micro pores within material structure.

- The measured dielectric properties of P(VdF- HFP)

# Chapter 5

# Manufacturing parameter variation

The final chapter investigates whether formulas can be obtained that predict the deposition rate, and the contact angle (of a deionised water droplet on a hydrophobic polymer) by making use of the variable process parameters in the fluoropolymer deposition process. For this investigation, 19 silicon wafers were coated with a fluoropolymer while varying the following process parameters:

- $C_4F_8$ flow (sccm)
- $CHF_3$ flow (sccm)
- Pressure (mTorr)
- Power bias (W)
- Frequency (Hz)

The samples were then tested to determine their deposition rate (material thickness/deposition time), using an ellipsometry test to determine material thickness, and the contact angle of a de-ionised water droplet on the layer surface using video-based optical contact angle meter (VOCAM). A statistical regression analysis is used to determine which process parameters played a role in these material characteristics. Finally, a formula is obtained that predicts the deposition rate of the material and the contact angle of the water droplet on the fluoropolymer.

## 5.1. Process parameter variation of fluoropolymer deposition

The characteristics of the 19 Si-wafers can be seen in Table 5.1 and the polymerisation process parameters for each wafer can be seen in Table 5.2 and Figure 5.1. Note that wafers 6, 10 and 11 have the same process parameters.

**Table 5.1:** Wafer Characteristics

| Material | Si-Wafer; 100 mm; Polished on one side |
|---|---|
| Specification | Siegert 111129-6492-1 |
| Wafer thickness | 525 µm |
| TTV | < 5 µm |
| Orientation | p(100) |
| Resistivity | < 0,01 Ωcm |

**Table 5.2:** Process parameter variation of fluoropolymer deposition of the 19 Si-wafers

| Wafer | Frequency (Hz) | Pressure (mTorr) | Power Bias (W) | $C_4F_8$ (sccm) | $CHF_3$ (sccm) |
|---|---|---|---|---|---|
| 1 | 380 | 10 | 28 | 150 | 71 |
| 2 | 380 | 60 | 28 | 150 | 0 |
| 3 | 13560 | 10 | 0 | 10 | 0 |
| 4 | 380 | 10 | 0 | 150 | 0 |
| 5 | 380 | 10 | 28 | 10 | 0 |
| 6 | 380 | 24.5 | 14 | 80 | 35.5 |
| 7 | 380 | 60 | 0 | 10 | 0 |
| 8 | 13560 | 10 | 12 | 10 | 71 |
| 9 | 13560 | 10 | 12 | 150 | 0 |
| 10 | 380 | 24.5 | 14 | 80 | 35.5 |
| 11 | 380 | 24.5 | 14 | 80 | 35.5 |
| 12 | 13560 | 60 | 12 | 150 | 71 |
| 13 | 13560 | 10 | 0 | 150 | 71 |
| 14 | 380 | 60 | 0 | 150 | 71 |
| 15 | 13560 | 60 | 0 | 150 | 0 |
| 16 | 380 | 10 | 0 | 10 | 71 |
| 17 | 380 | 60 | 28 | 10 | 71 |
| 18 | 13560 | 60 | 12 | 10 | 0 |
| 19 | 13560 | 60 | 0 | 10 | 71 |
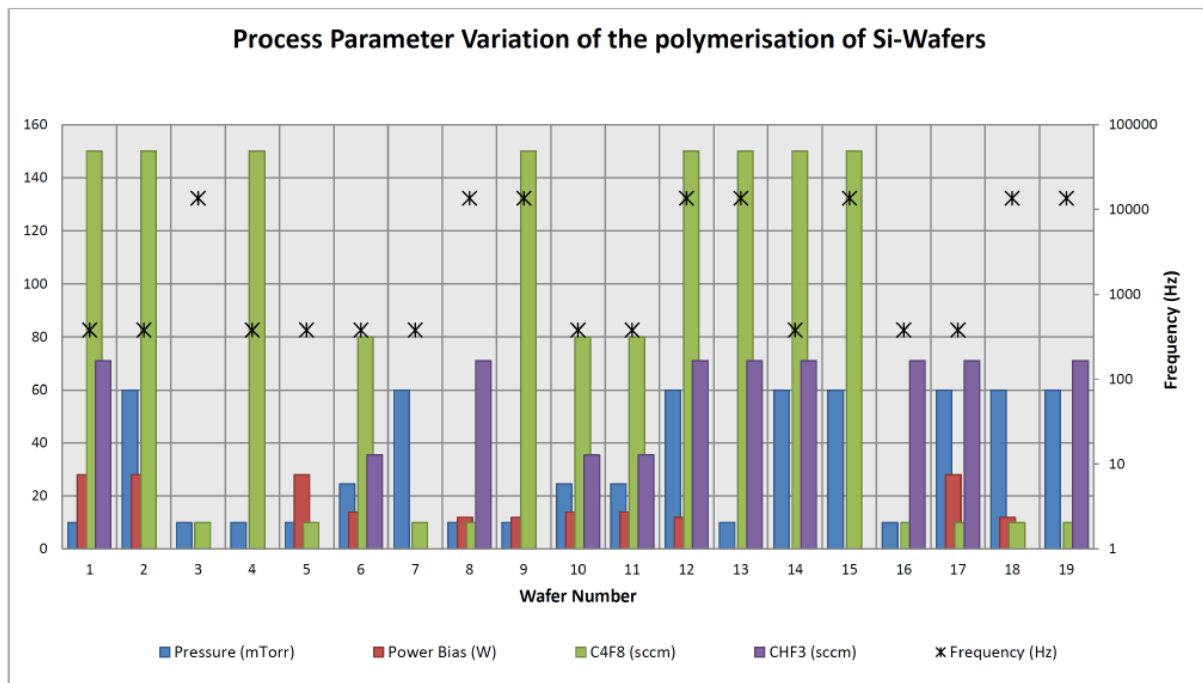


**Figure 5.1:** Graphic representation of the process parameter variation of fluoropolymer deposition of the 19 Si-wafers

## 5.2. Measurement of polymer deposition rate and droplet contact angle

### 5.2.1. Ellipsometry test results

In order to determine the radial variation of the polymerisation process, three test areas were selected, as can be seen in Figure 5.2. The ellipsometry test was conducted on the one half of the Si-wafers and the contact angle on the other, with the positions being mirrored in terms of radius from the cut-edge.
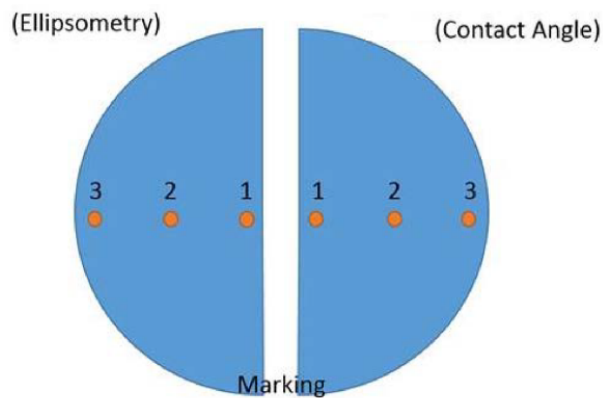


**Figure 5.2:** Testing positional markings

To determine the thickness of the polymer layer, an ellipsometry test was conducted by a laboratory assistant at Fraunhofer ENAS. The results are shown in Table 5.3. Also shown in Table 5.3 is the deposition time of the polymer layer and the calculated deposition rate.

**Table 5.3:** Ellipsometry results

| Wafer | Wafer thickness (nm) measured at Positions: | | | Wafer Average (nm) | Deposition Time (s) | Deposition Rate (nm/s) |
|---|---|---|---|---|---|---|
| | 1 | 2 | 3 | | | |
| 1 | 50.6 | 49.4 | 45.8 | 48.6 | 38 | 1.279 |
| 2 | 40.6 | 43.9 | 36.2 | 40.2 | 62 | 0.649 |
| 3 | 30.7 | 28.8 | 25.7 | 28.4 | 33 | 0.860 |
| 4 | 53.3 | 51.3 | 47.2 | 50.6 | 31 | 1.632 |
| 5 | 48.1 | 48.7 | 45.5 | 47.4 | 298 | 0.159 |
| 6 | **51.0** | **48.5** | **40.5** | **46.7** | **32** | **1.459** |
| 7 | 50.2 | 48.5 | 53.8 | 50.8 | 431 | 0.118 |
| 8 | 30.0 | 31.6 | 28.7 | 30.1 | 63 | 0.477 |
| 9 | 63.9 | 63.5 | 57.2 | 61.5 | 33 | 1.864 |
| 10 | **49.9** | **47.1** | **38.8** | **45.3** | **32** | **1.415** |
| 11 | **50.2** | **46.1** | **37.8** | **44.7** | **32** | **1.396** |
| 12 | 84.7 | 79.7 | 71.7 | 78.7 | 113 | 0.696 |
| 13 | 51.4 | 49.5 | 44.8 | 48.5 | 31 | 1.566 |
| 14 | 33.5 | 31.3 | 25.0 | 29.9 | 107 | 0.280 |
| 15 | 38.5 | 35.4 | 28.8 | 34.2 | 130 | 0.263 |
| 16 | 43.9 | 40.4 | 34.6 | 39.6 | 34 | 1.166 |
| 17 | 44.7 | 41.8 | 37.0 | 41.2 | 127 | 0.324 |
| 18 | 97.0 | 94.7 | 90.9 | 94.2 | 258 | 0.365 |
| 19 | 63.6 | 55.8 | 42.2 | 53.9 | 292 | 0.184 |

There is a lot of variation in the thickness of the polymer layer due to the variation in the process parameters. However, wafers 6,10,11 (indicated in Bold) has the same process parameters and the same deposition time, and there is consistency in the deposition rates of those 3 wafers. Figure 5.3 shows the ellipsometry test results for each position on the wafers. Figure 5.4 shows the variation of the wafers' average thickness, as well as the maximum and minimum error across the positions (See Figure 5.2) for each wafer.

**Figure 5.3:** Positional results of the of ellipsometry test showing the thickness of the polymer layer
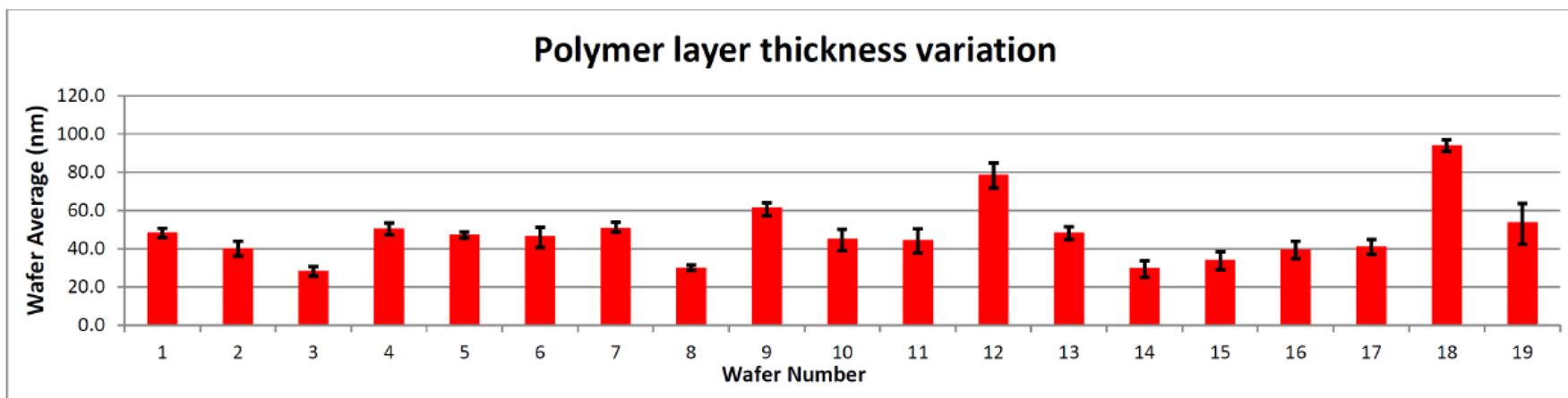
**Figure 5.4:** Ellipsometry results for the 19 samples showing average wafer thickness and maximum and minimum value error bars
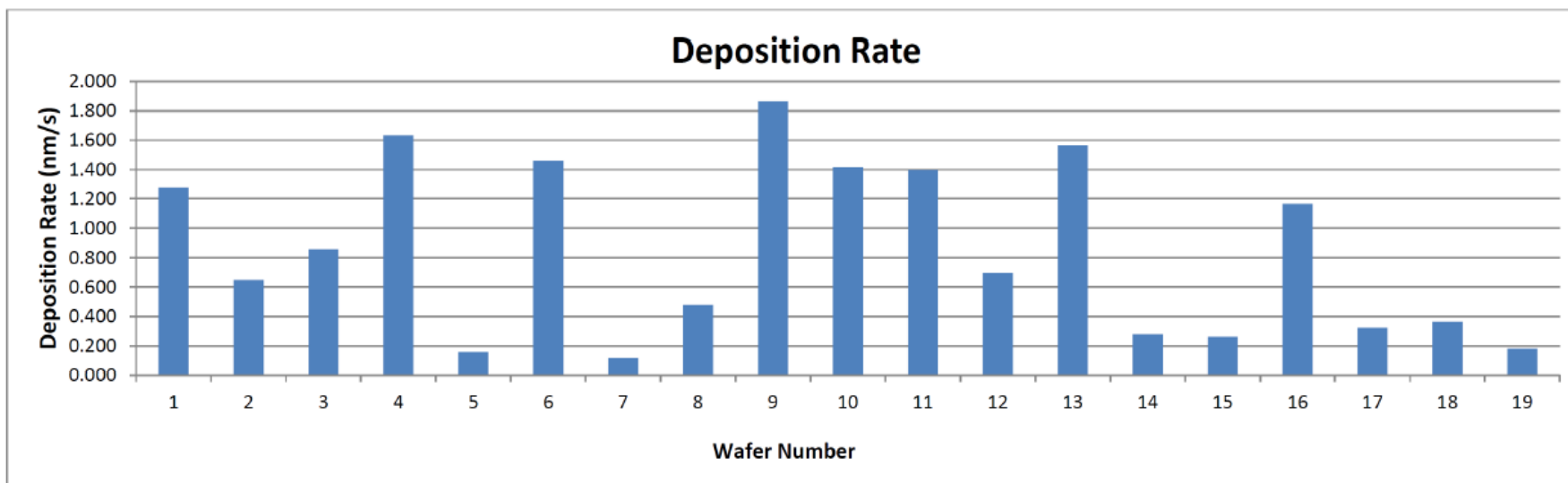


**Figure 5.5:** Deposition Rate of the 19 measured samples

## 5.3. Contact angle tests

Using the same technique and machinery discussed in Section 4.2, $1\mu l$-droplets of deionised water were deposited onto the surface of the polymer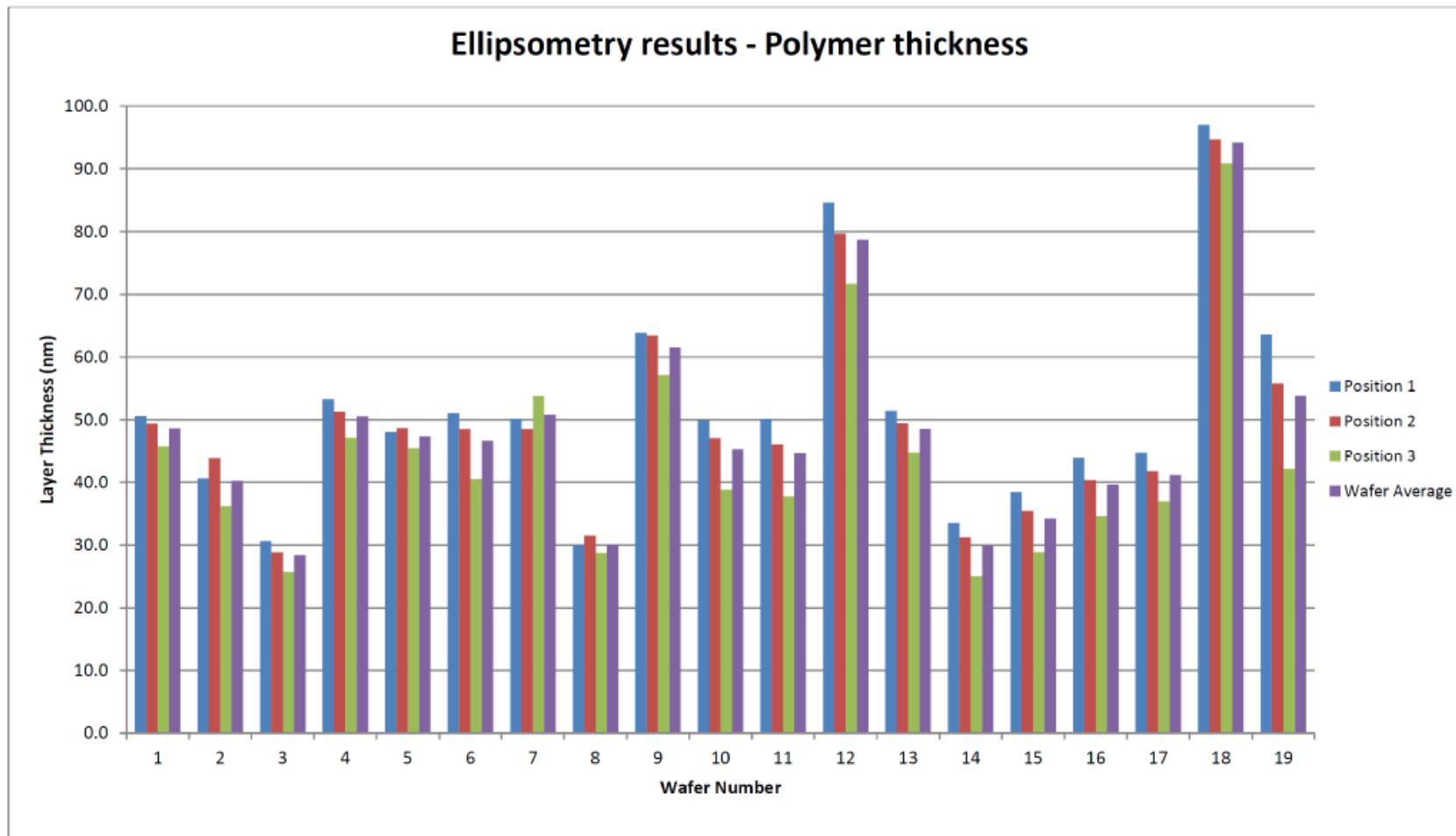 coated wafers before imaging the droplet and measuring the contact angle. A minimum of 6 drops were deposited on each of the three positions (see Figure 5.2), resulting in 740 individual measurements across the 19 wafers. The contact angles results are shown in Table 5.4 and Figure 5.6, with the error bars indicating the maximum and minimum measurements made for each position of every wafer.

**Table 5.4:** Averaged measurements of contact angles for each position on wafers 1-19

| Wafer | Position Average (nm) | | | Wafer Average (nm) |
|---|---|---|---|---|
| | Position 1 | Position 2 | Position 3 | |
| 1 | 111.6 | 107.3 | 111.4 | 110.1 |
| 2 | 104.4 | 108.3 | 110.0 | 107.6 |
| 3 | 113.1 | 112.5 | 113.7 | 113.1 |
| 4 | 112.0 | 112.9 | 112.1 | 112.3 |
| 5 | 113.1 | 112.8 | 111.5 | 112.5 |
| 6 | 112.2 | 109.7 | 106.2 | 109.4 |
| 7 | 42.4 | 39.6 | 36.5 | 39.5 |
| 8 | 112.7 | 112.0 | 108.7 | 111.1 |
| 9 | 106.3 | 109.8 | 110.2 | 108.7 |
| 10 | 108.5 | 108.9 | 108.4 | 108.6 |
| 11 | 109.5 | 110.7 | 109.7 | 110.0 |
| 12 | 103.5 | 104.6 | 104.9 | 104.3 |
| 13 | 111.6 | 112.6 | 112.0 | 112.0 |
| 14 | 104.3 | 106.1 | 106.7 | 105.7 |
| 15 | 106.3 | 107.6 | 108.4 | 107.4 |
| 16 | 113.0 | 114.0 | 113.3 | 113.4 |
| 17 | 111.2 | 111.7 | 111.5 | 111.5 |
| 18 | 109.3 | 110.8 | 110.0 | 110.0 |
| 19 | 111.1 | 111.8 | 111.9 | 111.6 |

Wafer 7 was subjected to both the CF-Polymer deposition process, as well as a $O_2$-plasma cleaning process. This reduced the nano-roughness of the polymer surface, with the resulting surface roughness changing the hydrophobicity of the polymer layer from hydrophobic to hydrophilic. This phenomenon was also observed by Loong et al. [56]. For the purposes of establishing relationships between the process parameters and the measured contact angle, Wafer 7 will be excluded to avoid the anomaly in the data set.
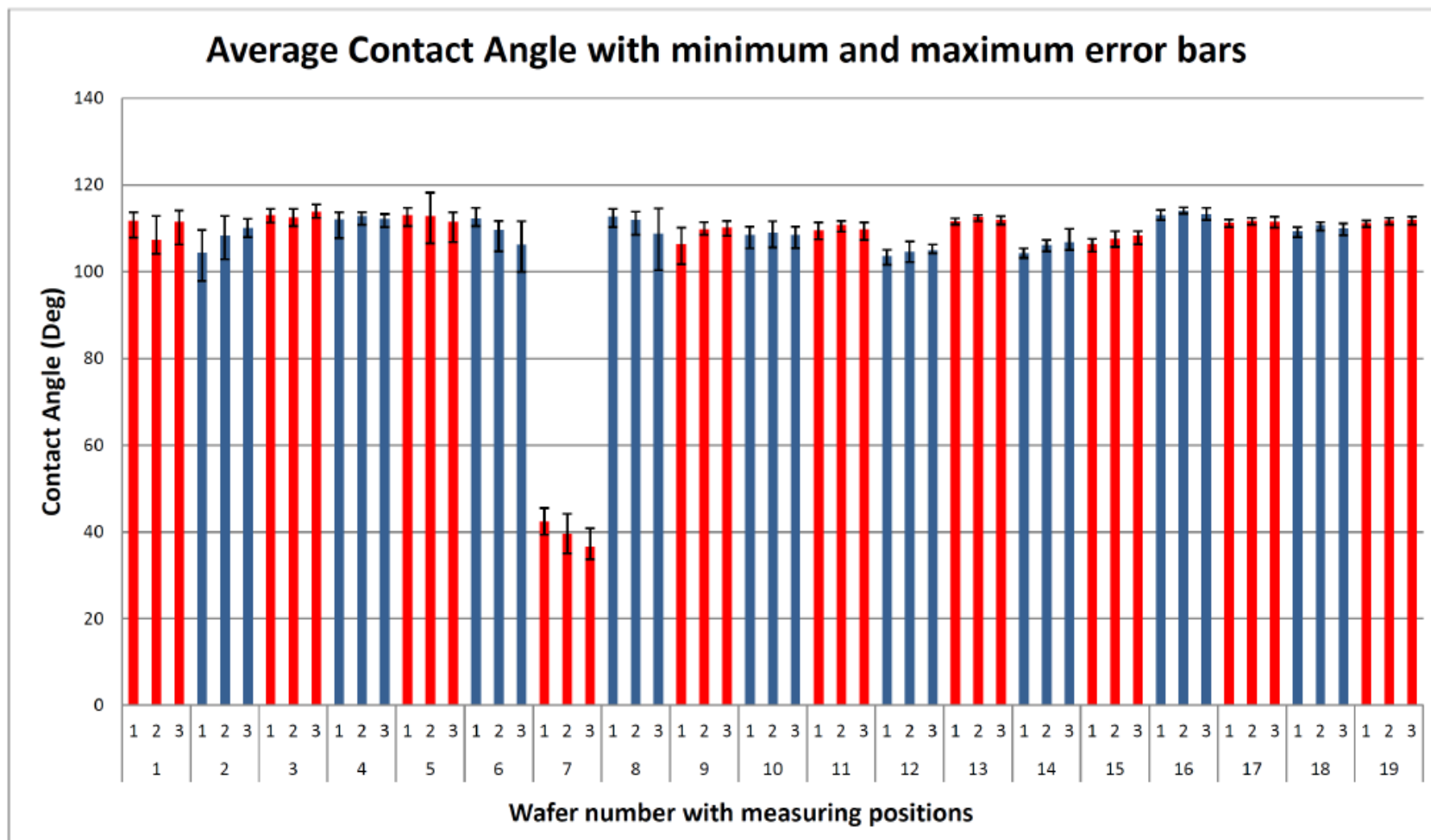
**Figure 5.6:** Average contact angle measurement results showing the maximum and minimum measured values with the error bars

# 5.4. Comparing the test results with process parameters

To compare the test results with the process parameters, the average contact angle and the rate of deposition were selected to compare with the process parameters. To determine the relationships mathematically, a regression analysis was done. The regression analysis was done in Microsoft Excel using the Solver Add-in. Wafer 7 was excluded from the comparison due to it being an anomaly and would statistically skew the results.

## 5.4.1. Comparison of contact angle and process parameters

For figures 5.7 & 5.8, the 18 measurements of contact angle is compared to the various process parameters. As can be seen from the trend line and the relatively higher $R^2$ value in the bottom left corner of the figures, only the $C_4F_8$ gas and the pressure has some relation to the resulting contact angle. However, with $R^2$ values of less than 0.4, these process parameters do not strongly predict the contact angle by themselves.
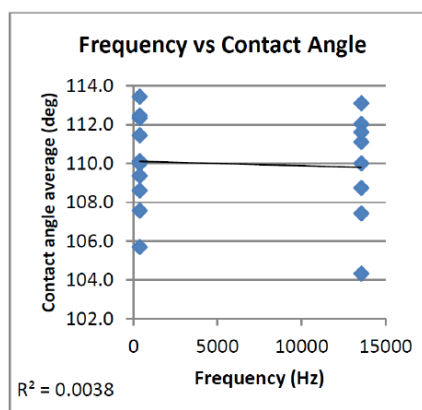


**Figure 5.7:** Frequency vs contact angle
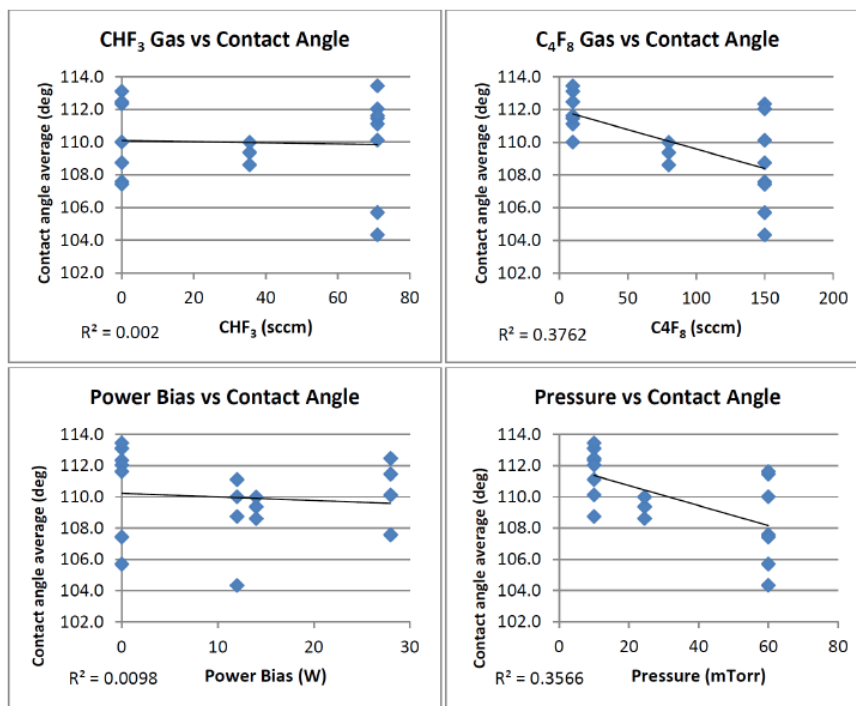


**Figure 5.8:** Varying process parameters vs contact angle

Using the Solver tool, two equations for the predicted contact angle were obtained. First, using all of the process parameters as variables and then, only the $C_4F_8$ gas and the pressure as variables, being the two parameters with the highest $R^2$ values.

The two approximations, or predictions Pred 1 and Pred 2, are shown in Table 5.5. The columns marked err, represent the error-squared value between the real measured value and the predicted value ie. err = (Contact angle average (deg) - Pred)$^2$. The Solver platform was programmed to find the minimum value of the sum of all the err-values by adjusting the coefficients of the selected variables, seen in Table 5.6. This method selects the optimal coefficients of the variables (process parameters) for a prediction of the contact angle that is nearest to the measured values. The colour bands can be used to see the similarities of the predictions to the measured values.

**Table 5.5:** Contact angle prediction results of regression analysis

| Wafer | Contact angle average (deg) | Pred 1 | res1 | err 1 | pred 2 | res2 | err 2 |
|---|---|---|---|---|---|---|---|
| 1 | 110.1 | 109.1111 | 1.01 | 1.016792 | 109.8056 | 0.31 | 0.098478 |
| 2 | 107.6 | 106.6204 | 0.95 | 0.904468 | 106.823 | 0.75 | 0.560158 |
| 3 | 113.1 | 113.2371 | -0.13 | 0.01775 | 112.9132 | 0.19 | 0.036374 |
| 4 | 112.3 | 110.5327 | 1.81 | 3.276561 | 109.8056 | 2.54 | 6.437107 |
| 5 | 112.5 | 112.6915 | -0.22 | 0.049419 | 112.9132 | -0.44 | 0.19711 |
| 6 | 109.4 | 110.6144 | -1.25 | 1.554379 | 110.4944 | -1.13 | 1.269755 |
| 8 | 111.1 | 112.4287 | -1.32 | 1.739062 | 112.9132 | -1.80 | 3.251733 |
| 9 | 108.7 | 109.5455 | -0.80 | 0.640346 | 109.8056 | -1.06 | 1.124306 |
| 10 | 108.6 | 110.6144 | -2.00 | 4.012656 | 110.4944 | -1.88 | 3.546624 |
| 11 | 110.0 | 110.6144 | -0.63 | 0.391137 | 110.4944 | -0.51 | 0.255527 |
| 12 | 104.3 | 106.3575 | -2.03 | 4.117674 | 106.823 | -2.49 | 6.223319 |
| 13 | 112.0 | 109.6567 | 2.38 | 5.671061 | 109.8056 | 2.23 | 4.983891 |
| 14 | 105.7 | 107.3447 | -1.65 | 2.719591 | 106.823 | -1.13 | 1.271112 |
| 15 | 107.4 | 107.166 | 0.27 | 0.070407 | 106.823 | 0.61 | 0.370099 |
| 16 | 113.4 | 113.4158 | 0.03 | 0.000723 | 112.9132 | 0.53 | 0.280367 |
| 17 | 111.5 | 109.5035 | 1.95 | 3.800148 | 109.9305 | 1.52 | 2.317685 |
| 18 | 110.0 | 109.938 | 0.07 | 0.004568 | 109.9305 | 0.08 | 0.005628 |
| 19 | 111.6 | 110.0491 | 1.57 | 2.461101 | 109.9305 | 1.69 | 2.84732 |
| | | SUM | 0.0008 | 32.44784 | SUM | 1.37E-05 | 35.07659 |

**Table 5.6:** Variables and coefficients of the contact angle prediction

| | Variables: | Constant | Frequency (Hz) | Pressure (mTorr) | Power Bias (W) | $C_4F_8$ (sccm) | $CHF_3$ (sccm) |
|---|---|---|---|---|---|---|---|
| Pred 1 | Partial regression coefficients: | 114.5783 | -4E-05 | -0.05679 | -0.03832 | -0.02308 | -0.00491047 |
| | Variables: | Constant | Frequency (Hz) | Pressure (mTorr) | Power Bias (W) | $C_4F_8$ (sccm) | $CHF_3$ (sccm) |
| Pred 2 | Partial regression coefficients: | 113.7317 | 0 | -0.05965 | 0 | -0.0222 | 0 |

Figure 5.9(a) shows the scatter plotting of the results of the Pred 1 and Pred 2 formula compared to the actual measured results of the contact angles. Note that Pred 1 has the higher $R^2$ value and thus, better predicts the contact angle. This can also be seen in Figure 5.9(b), where Res 1, showing the residuals of the Pred 1 predictions, has the lowest $R^w$ value, also indicating the nearest approximation to the actual measurements.
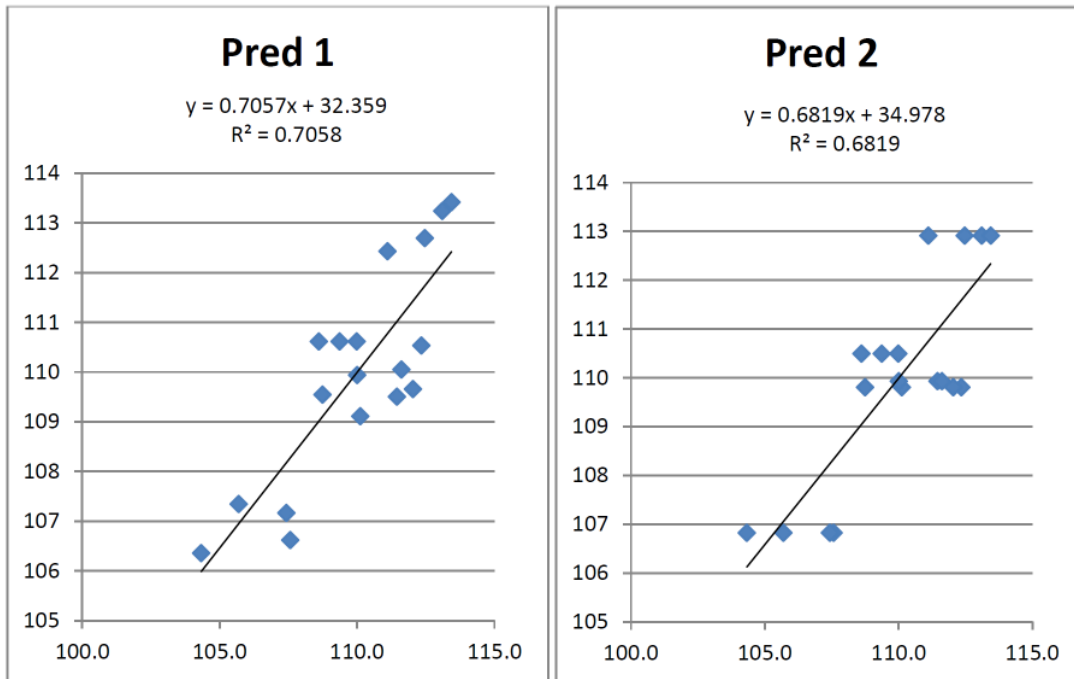


**(a)** Prediction results
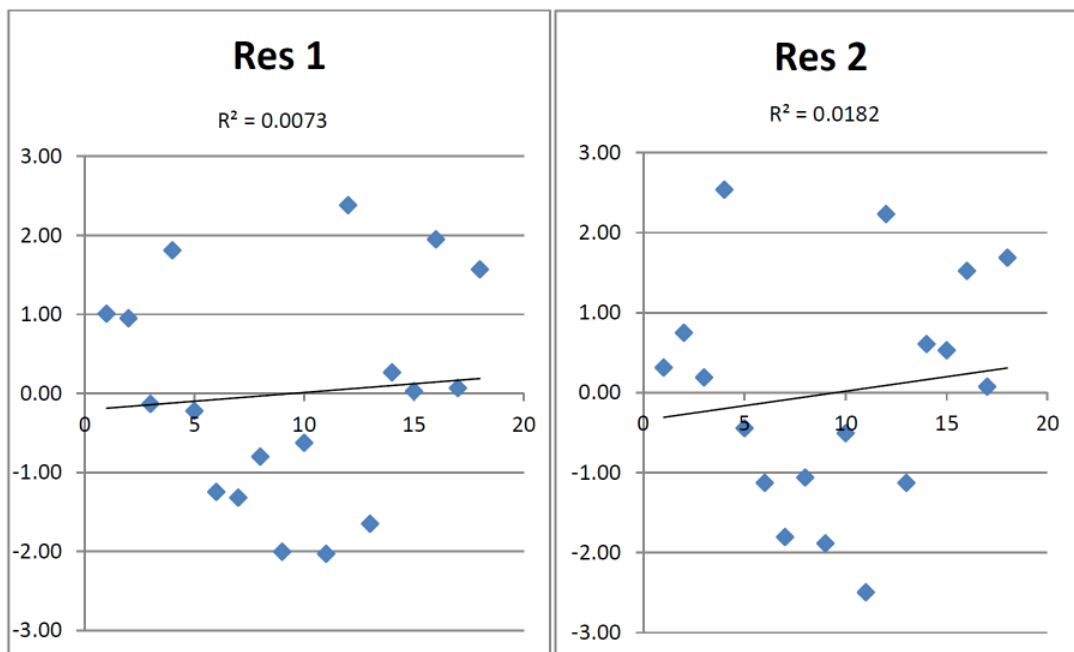


**(b)** Residual results

**Figure 5.9:** Predictions and residuals from regression analysis to approximate the contact angle from the process parameters set during fabrication

## 5.4.2. Comparison of deposition rate and process parameters

Similar to the the previous section, the values of the deposition rate, for each wafer, are compared to the various process parameters, as well as the results of the contact angle measurements. These comparisons are shown in Figure 5.10 where the trend lines and $R^2$ values give an indication as to how indicative the specific parameter is of the resulting deposition rate. A high $R^2$ value indicates a strong correlation. It can also be seen that there is no strong correlation between the deposition rate and the measured contact angle.
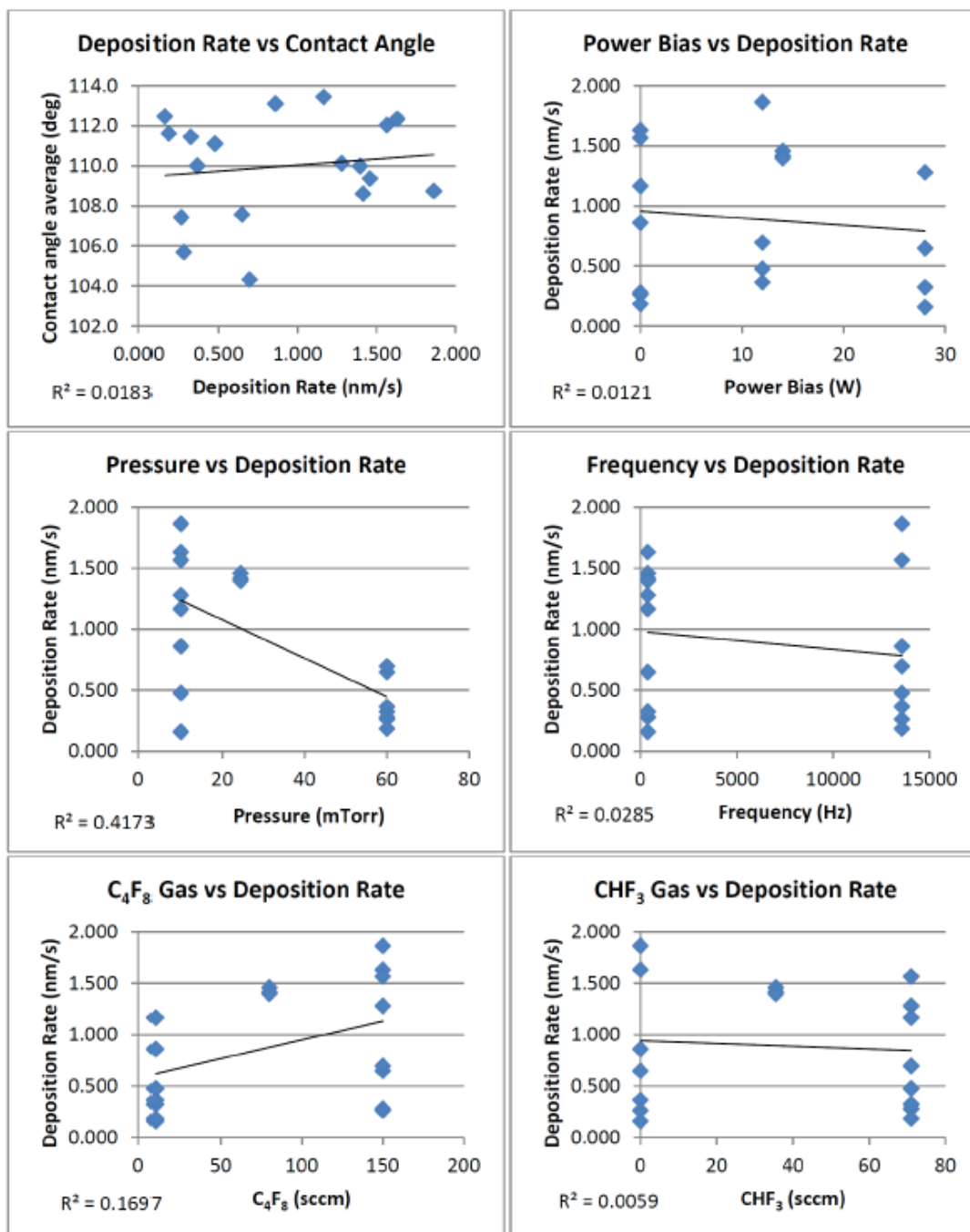


**Figure 5.10:** Process variables vs deposition rate

A regression analysis was done to predict the deposition rate by assigning and optimising coefficients to the variables (process parameters). This time, four predictions (Pred1 - Pred4) were obtained using this method, first using all of the variables together with the constant, and then progressively eliminating the variable with the lowest $R^2$ value. The results of the four predictions seen in Table 5.7 and Table 5.8. The colour bands can be used to see the similarities of the predictions to the measured values.

**Table 5.7:** Deposition rate prediction results of regression analysis

| Deposition Rate (nm/s) | Pred 1 | res1 | err 1 | pred 2 | res2 | err 2 | pred 3 | res3 | err 3 | pred 4 | res4 | err 4 |
|---|---|---|---|---|---|---|---|---|---|---|---|---|
| 1.279 | 1.495 | -0.217 | 0.047 | 1.491 | -0.213 | 0.045 | 1.564 | -0.285 | 0.081 | 1.525 | -0.246 | 0.060 |
| 0.649 | 0.659 | -0.011 | 0.000 | 0.663 | -0.015 | 0.000 | 0.726 | -0.077 | 0.006 | 0.692 | -0.043 | 0.002 |
| 0.860 | 0.934 | -0.074 | 0.005 | 0.938 | -0.078 | 0.006 | 0.896 | -0.036 | 0.001 | 0.953 | -0.093 | 0.009 |
| 1.632 | 1.605 | 0.026 | 0.001 | 1.609 | 0.022 | 0.000 | 1.564 | 0.068 | 0.005 | 1.525 | 0.107 | 0.011 |
| 0.159 | 0.916 | -0.757 | 0.573 | 0.920 | -0.761 | 0.578 | 0.981 | -0.822 | 0.676 | 0.953 | -0.794 | 0.630 |
| 1.459 | 1.024 | 0.434 | 0.189 | 1.024 | 0.434 | 0.189 | 1.029 | 0.429 | 0.184 | 0.997 | 0.461 | 0.213 |
| 0.118 | 0.205 | -0.087 | 0.008 | 0.209 | -0.091 | 0.008 | 0.143 | -0.025 | 0.001 | 0.120 | -0.002 | 0.000 |
| 0.477 | 0.891 | -0.414 | 0.171 | 0.887 | -0.410 | 0.168 | 0.896 | -0.419 | 0.176 | 0.953 | -0.476 | 0.226 |
| 1.864 | 1.455 | 0.409 | 0.167 | 1.459 | 0.405 | 0.164 | 1.479 | 0.385 | 0.148 | 1.525 | 0.339 | 0.115 |
| 1.415 | 1.024 | 0.391 | 0.153 | 1.024 | 0.391 | 0.153 | 1.029 | 0.386 | 0.149 | 0.997 | 0.418 | 0.175 |
| 1.396 | 1.024 | 0.372 | 0.138 | 1.024 | 0.372 | 0.138 | 1.029 | 0.367 | 0.134 | 0.997 | 0.399 | 0.159 |
| 0.696 | 0.635 | 0.061 | 0.004 | 0.631 | 0.065 | 0.004 | 0.641 | 0.056 | 0.003 | 0.692 | 0.004 | 0.000 |
| 1.566 | 1.513 | 0.052 | 0.003 | 1.510 | 0.056 | 0.003 | 1.479 | 0.087 | 0.008 | 1.525 | 0.041 | 0.002 |
| 0.280 | 0.785 | -0.506 | 0.256 | 0.781 | -0.502 | 0.252 | 0.726 | -0.446 | 0.199 | 0.692 | -0.413 | 0.170 |
| 0.263 | 0.678 | -0.414 | 0.172 | 0.681 | -0.418 | 0.175 | 0.641 | -0.377 | 0.142 | 0.692 | -0.429 | 0.184 |
| 1.166 | 1.041 | 0.124 | 0.015 | 1.037 | 0.128 | 0.016 | 0.981 | 0.184 | 0.034 | 0.953 | 0.213 | 0.045 |
| 0.324 | 0.095 | 0.229 | 0.052 | 0.092 | 0.233 | 0.054 | 0.143 | 0.181 | 0.033 | 0.120 | 0.204 | 0.042 |
| 0.365 | 0.055 | 0.310 | 0.096 | 0.059 | 0.306 | 0.094 | 0.058 | 0.307 | 0.094 | 0.120 | 0.245 | 0.060 |
| 0.184 | 0.114 | 0.071 | 0.005 | 0.110 | 0.075 | 0.006 | 0.145 | 0.039 | 0.002 | 0.120 | 0.064 | 0.004 |
| | SUM | 0.000 | 2.054 | SUM | 0.000 | 2.054 | SUM | 0.000 | 2.075 | SUM | 0.000 | 2.107 |

**Table 5.8:** Variables and coefficients of the deposition rate prediction

| | variables: | Constant | Frequency (Hz) | Pressure (mTorr) | Power Bias (W) | $C_4F_8$ (sccm) | $CHF_3$ (sccm) |
|---|---|---|---|---|---|---|---|
| Pred 1 | partial regression coefficients: | 1.161112 | -7.6E-06 | -0.01656 | -0.00421 | 0.004084 | 0.000111 |
| | variables: | Constant | Frequency (Hz) | Pressure (mTorr) | Power Bias (W) | $C_4F_8$ (sccm) | $CHF_3$ (sccm) |
| Pred 2 | partial regression coefficients: | 1.165009 | -7.6E-06 | -0.01656 | -0.00421 | 0.004084 | 0 |
| | variables: | Constant | Frequency (Hz) | Pressure (mTorr) | Power Bias (W) | $C_4F_8$ (sccm) | $CHF_3$ (sccm) |
| Pred 3 | partial regression coefficients: | 1.10963 | -6.4E-06 | -0.01676 | 0 | 0.004162 | 0 |
| | variables: | Constant | Frequency (Hz) | Pressure (mTorr) | Power Bias (W) | $C_4F_8$ (sccm) | $CHF_3$ (sccm) |
| Pred 4 | partial regression coefficients: | 1.078396 | 0 | -0.01665 | 0 | 0.004084 | 0 |

**Figure 5.11:** Results of the four prediction equations
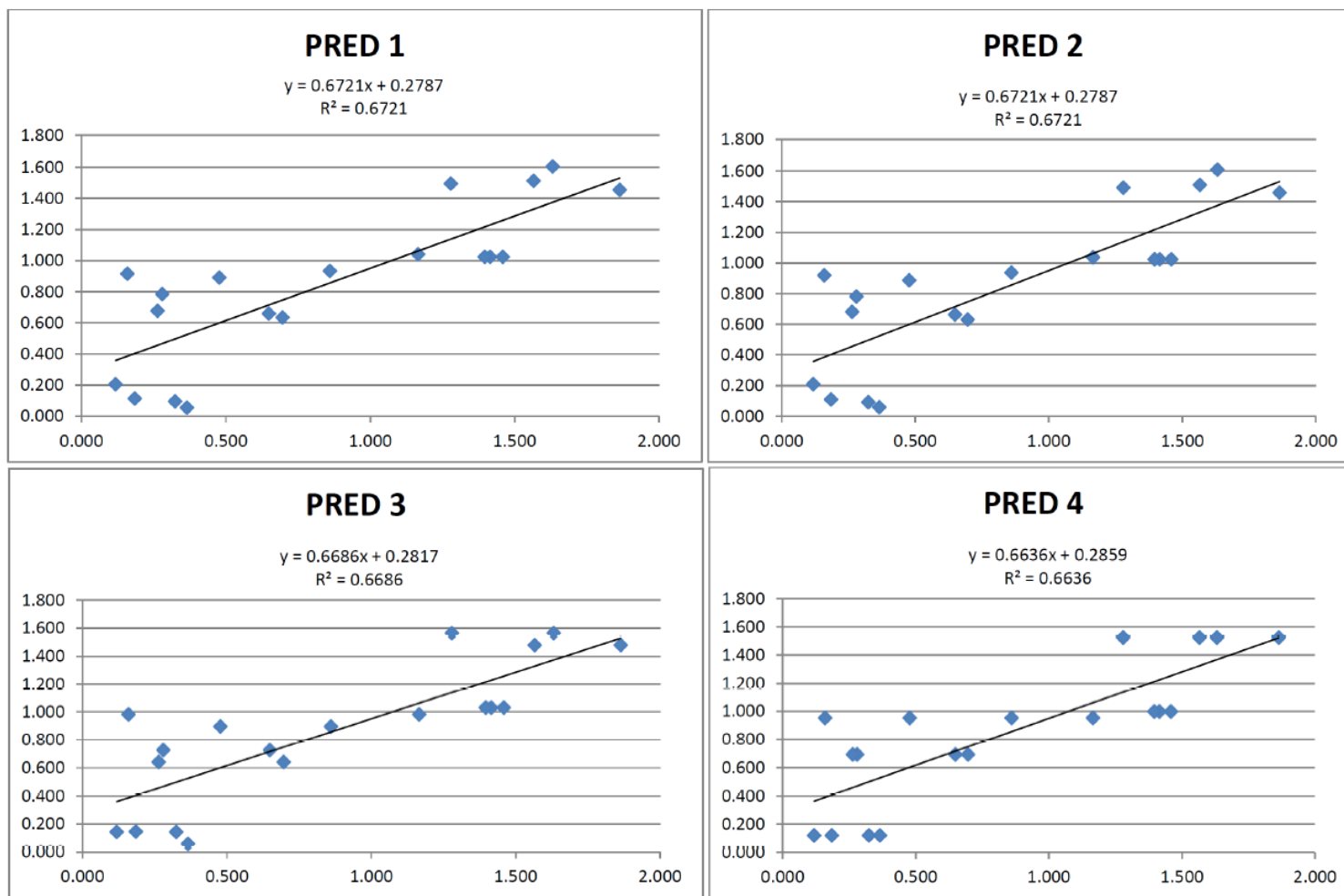
Of the four predictions, Pred 1 and Pred 2 yielded practically identical results, as the coefficient of the $CHF_3$ gas flow rate was set to 0.000111 in Pred 1 and 0 in Pred 2.
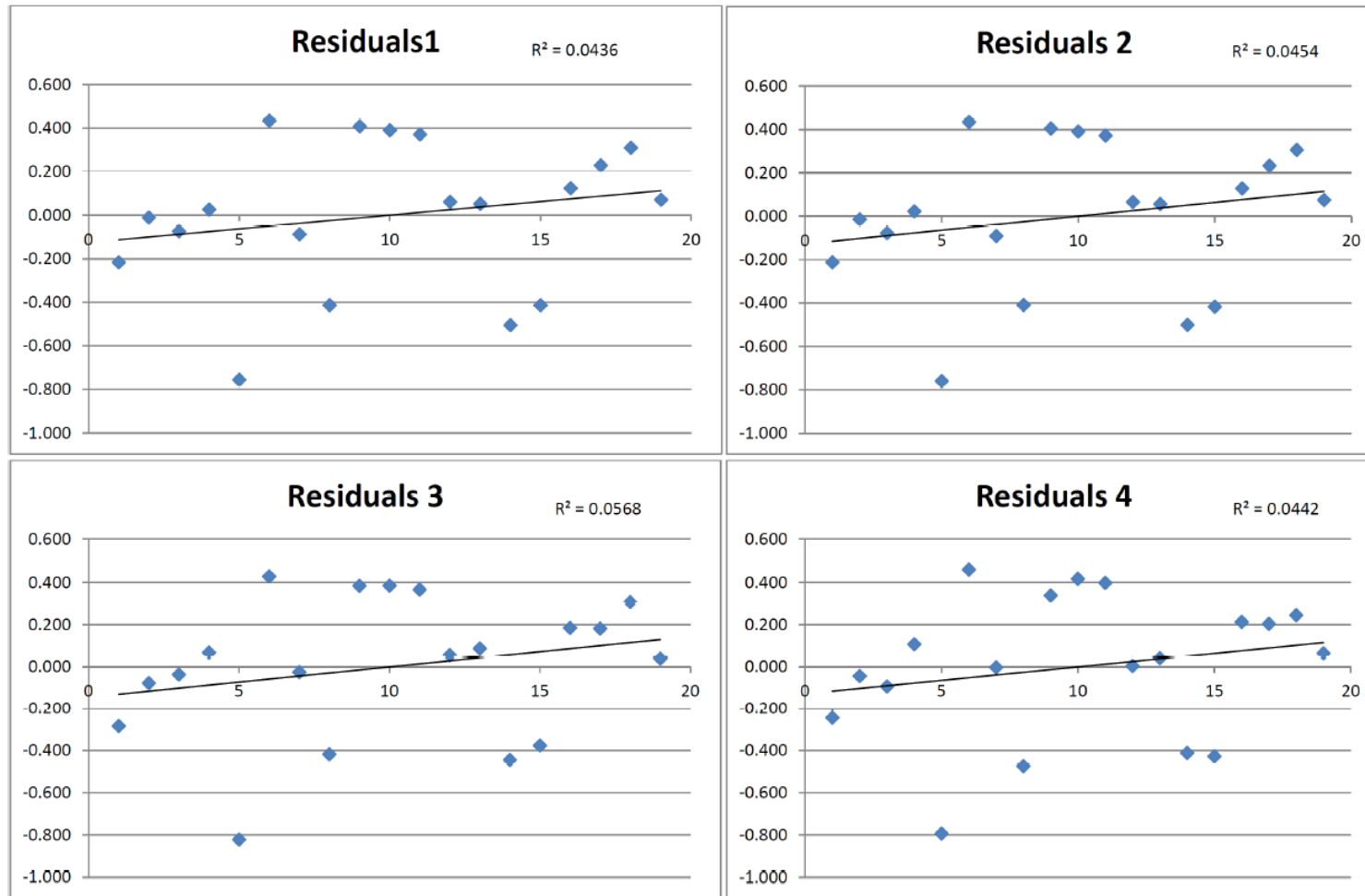
**Figure 5.12:** Residuals of deposition rate predictions

The residual values are really similar for Pred 1, Pred 2 and Pred 4. But Pred 1 does yield the residuals with the lowest $R^2$ value.

### 5.4.3. Discussion of regression analysis results

Although a sample group of 19 is too small to draw statistically significant conclusions, the regression analysis approach does set a platform for future experiments to establish a formula for predicting deposition rate or perhaps contact angle of samples coated with this fluoropolymer.

In figures 5.9(a) & 5.11, it can be seen that for both the contact angle and deposition rate predictions, there is not much improvement when eliminating the variables that have a weak correlation to the measured result, albeit contact angle or deposition rate. The residual graphs 5.9(b) & 5.12 all show a random distribution, which indicates that the all the predictions yielded results that had good approximations to the measured values.

Based on the analysis, the contact angle can be approximated by

$$\text{Contact Angle (deg)} = 96.89312 + 0.0008219f - 0.2511P_r + 0.5004P_o$$
$$+ 0.04069G_{C4F8} + 0.12084G_{CHF3} \tag{5.1}$$

where $f$ is the frequency (Hz), $P_r$ is Pressure (mTorr), $P_o$ is Power Bias (W), $G_{C4F8}$ is $C_4F_8$ flow rate (sccm) and $G_{CHF3}$ is $CHF_3$ flow rate (sccm), and the deposition rate by

$$\text{Deposition Rate (nm/s)} = 1.1611 - 7.54693249f - 0.01656P_r - 0.00420P_o$$
$$+ 0.004084G_{C4F8} + 0.00010979G_{CHF3} \tag{5.2}$$

Both of the equations consists of a constant integer followed by the various process variables, multiplied by the optimised coefficients, obtained from the solver tool. These formulas can be adjusted using the coefficients of the various predictions. With more tested samples in the future, a more accurate formula can be obtained. It could then be demonstrated that predictions can in fact be made from these process parameters. This will enable samples to be prepared with process parameters set for an optimal hydrophobic contact angle.

# 5.5. Summary

A summary of the observations made from the various tests, as well the the recommendations for future tests are given in Table 5.9.

**Table 5.9:** Observations and recommendations for future tests on the hydrophobic CF-polymer

|  | **Observations and conclusions** | **Recommendations for future tests** |
|---|---|---|
| **Process parameter variation** | The process parameters were varied for the 19 Si-wafers. Wafers 6, 10 and 11 have the same process parameters and yielded similar deposition rates. This indicates some reproducibility, but a sample of three is not large enough to draw statistical conclusions. | Future tests should include more groups with identical process parameters to test whether similar deposition rates can be achieved. |
| **Ellipsometry tests** | The thickness of the polymer layer tended to decrease from position 1 to position 3, indicating that the layer is deposited thickest in the centre of the wafer and reduces in thickness towards the edge. | Investigate the impact of layer thickness on contact angle behaviour further to establish whether samples can be cut from the same wafer (with variating thicknesses) to be used in LADM devices. |
| **Contact angle tests** | The contact angle tests showed that the polymer layer displayed hydrophobic behaviours with contact angles between $104^{\circ}$ and $113^{\circ}$. Wafer 7 was treated with an $O_2$-plasma cleaning process, which changed the nano-roughness of the material. This in turn changed the hydrophobicity of the sample to hydrophilic. | The process to create the hydrophilic layer should be replicated at least once more to confirm that the $O_2$-plasma cleaning process is indeed responsible for altering the surface roughness. The use of an AFM microscope is recommended to measure the surface roughness. |
| **Regression analysis** | With only 19 samples to test, no certain conclusions can be made. However, there does seem to be potential for using the formulas obtained by the analysis to set the process parameters according to the required rate of deposition or contact angle. | The use of additional samples to increase the data set and improve on the formulas obtained from the regression analysis is recommended. |

# Chapter 6

# Summary and Conclusion

## General discussion

This research aimed to identify polymer materials that are suitable as functional layers in a LADM device. Based on a quantitative analysis where critical material properties and performance characteristics of the polymer materials are tested, it can be concluded that the photoconductive properties of P3HT:PCBM, the dielectric and hydrophobic properties of P(VDF-HFP), and the hydrophobic properties of the fluoropolymer indicates their suitability for use in LADM devices.

While the amount of samples used in the study in Chapter 3 and Chapter 4 somewhat limits the generalisability of the results, the instrumentation and methods used does provide credibility to the research findings. The statistical approach used in Chapter 5 for the regression analysis proves to be a useful tool to determine the optimal inputs for the fabrication parameters of the fluoropolymer. With over 740 measurements made in the contact angle tests, the results of Chapter 5 are statistically significant.

## Interpretations and recommendations for future work

The varying resistance measurements obtained from samples M18 and M20, discussed in Chapter 3, are attributed to the uneven layer thickness of the samples. These results could then further be attributed to the spin coating process, where the polymer fluid was either not a completely homogenous mixture, or the chosen RPM was not sufficient for a layer of consistent thickness. A similar conclusion can be hypothesised for the variance of the contact angles reported in Chapter 4. From literature and from the results obtained in Chapter3 and Chapter 4 the correlations between fabrication strategies, surface morphology and apparent material properties is an important conclusion to note.

Based on these conclusions, researchers should consider adding nanoparticles to the P(VDF-HFP) before spin coating. The literature suggests that these additions will add to the surface roughness of the crystal structure, thereby further increasing its hydrophobic qualities. To better understand the impact of laser illumination on the P3HT:PCBM

photoconductive polymer, future studies could address the relationship of temperature and resistance in the material.

More detailed recommendations for future work can be found at the end of chapters 3, 4 and 5.

**Contributions to research**

In the broader context of microfluidic research, the introduction of new materials and their potential uses have systematically created the platform for new microfluidic devices. In doing so, these devices have introduced new solutions for existing problems in the fields of molecular analysis, biodefence, molecular biology and microelectronics.

The research of this project introduces novel research on two materials, yet untested in their use in LADM devices. The results are promising and indicate their suitability to be used in future research projects and potentially to be the materials chosen for prototyping and later, commercialisation.

# Bibliography

[1] Mendeley, "Websearch," 2020. [Online]. Available: https://www.mendeley.com/search

[2] H. T. Nguyen, H. Thach, E. Roy, K. Huynh, and C. M. T. Perrault, "Low-cost, accessible fabrication methods for microfluidics research in low-resource settings," *Micromachines*, vol. 9, no. 9, pp. 1–10, 2018.

[3] Y. Wang, S. Chen, H. Sun, W. Li, C. Hu, and K. Ren, "Recent progresses in microfabricating perfluorinated polymers (Teflons) and the associated new applications in microfluidics," *Microphysiological Systems*, vol. 1, no. November, pp. 1–1, 2018.

[4] C. W. Tsao, "Polymer microfluidics: Simple, low-cost fabrication process bridging academic lab research to commercialized production," *Micromachines*, vol. 7, no. 12, 2016.

[5] G. M. Whitesides, "The origins and the future of microfluidics," *Nature*, vol. 442, no. 7101, pp. 368–373, 2006.

[6] D. Mark, S. Haeberle, G. Roth, F. V. Stetten, and R. Zengerle, "Microfluidic lab-on-a-chip platforms: Requirements, characteristics and applications," *Chemical Society Reviews*, vol. 39, no. 3, pp. 1153–1182, 2010.

[7] G. A. Posthuma-Trumpie, J. Korf, and A. Van Amerongen, "Lateral flow (immuno)assay: Its strengths, weaknesses, opportunities and threats. A literature survey," *Analytical and Bioanalytical Chemistry*, vol. 393, no. 2, pp. 569–582, 2009.

[8] K. A. Erickson and P. Wilding, "Evaluation of a novel point-of-care system, the i-STAT Portable Clinical Analyzer," *Clinical Chemistry*, vol. 39, no. 2, pp. 283–287, 1993.

[9] U. M. Attia, S. Marson, and J. R. Alcock, "Micro-injection moulding of polymer microfluidic devices," 2009.

[10] B. S. Karon, R. D. McBane, R. Chaudhry, L. K. Beyer, and P. J. Santrach, "Accuracy of capillary whole blood international normalized ratio on the CoaguChek S, CoaguChek XS, and i-STAT 1 point-off-care analyzers," *American Journal of Clinical Pathology*, vol. 130, no. 1, 2008.

[11] E. Jacobs, E. Vadasdi, L. Sarkozi, and N. Colman, "Analytical evaluation of i-STAT Portable Clinical Analyzer and use by nonlaboratory health-care professionals," *Clinical Chemistry*, vol. 39, no. 6, 1993.

[12] G. Valet, "Past and present concepts in flow cytometry: A European perspective," 2003.

[13] D. Huh, W. Gu, Y. Kamotani, J. B. Grotberg, and S. Takayama, "Microfluidics for flow cytometric analysis of cells and particles," 2005.

[14] A. F. Sauer-Budge, P. Mirer, A. Chatterjee, C. M. Klapperich, D. Chargin, and A. Sharon, "Low cost and manufacturable complete microTAS for detecting bacteria," *Lab on a Chip*, vol. 9, no. 19, 2009.

[15] P. A. Auroux, Y. Koc, A. DeMello, A. Manz, and P. J. Day, "Miniaturised nucleic acid analysis," *Lab on a Chip*, vol. 4, no. 6, pp. 534–546, 2004.

[16] P. S. Dittrich, K. Tachikawa, and A. Manz, "Micro total analysis systems. Latest advancements and trends," 2006.

[17] N. Pamme and C. Wilhelm, "Continuous sorting of magnetic cells via on-chip free-flow magnetophoresis," *Lab on a Chip*, vol. 6, no. 8, 2006.

[18] L. Chen, A. Manz, and P. J. R. Day, "Total nucleic acid analysis integrated on microfluidic devices," 2007.

[19] C. J. Easley, J. M. Karlinsey, J. M. Bienvenue, L. A. Legendre, M. G. Roper, S. H. Feldman, M. A. Hughes, E. L. Hewlett, T. J. Merkel, J. P. Ferrance, and J. P. Landers, "A fully integrated microfluidic genetic analysis system with sample-in-answer-out capability," *Proceedings of the National Academy of Sciences of the United States of America*, vol. 103, no. 51, 2006.

[20] R. Society and P. Sciences, "Dispersion of Soluble Matter in Solvent Flowing Slowly through a Tube Author ( s ): Geoffrey Taylor Source : Proceedings of the Royal Society of London . Series A , Mathematical and Physical Published by : Royal Society Stable URL : http://www.jstor.org/s," vol. 219, no. 1137, pp. 186–203, 1953.

[21] N. Inui, "Relationship between contact angle of liquid droplet and light beam position in optoelectrowetting," *Sensors and Actuators, A: Physical*, vol. 140, no. 1, pp. 123–130, 2007.

[22] S. Y. Teh, R. Lin, L. H. Hung, and A. P. Lee, "Droplet microfluidics," *Lab on a Chip*, vol. 8, no. 2, pp. 198–220, 2008.

[23] S. Begolo, G. Colas, L. Malaquin, and J. L. Viovy, "Production of fluoropolymer microchips for droplet microfluidics and DNA amplification," *ASME 2010 8th International Conference on Nanochannels, Microchannels, and Minichannels Collocated with 3rd Joint US-European Fluids Engineering Summer Meeting, ICNMM2010*, no. PARTS A AND B, pp. 893–898, 2010.

[24] K. Choi, A. H. C. Ng, R. Fobel, and A. R. Wheeler, "Digital microfluidics," *Annual Review of Analytical Chemistry*, vol. 5, pp. 413–440, 2012.

[25] S. K. Cho, H. Moon, and C. J. Kim, "Creating, transporting, cutting, and merging liquid droplets by electrowetting-based actuation for digital microfluidic circuits," *Journal of Microelectromechanical Systems*, vol. 12, no. 1, pp. 70–80, 2003.

[26] F. Mugele and J. C. Baret, "Electrowetting: From basics to applications," 2005.

[27] J. Lee, H. Moon, J. Fowler, T. Schoellhammer, and C. J. Kim, "Electrowetting and electrowetting-on-dielectric for microscale liquid handling," *Sensors and Actuators, A: Physical*, vol. 95, no. 2-3, 2002.

[28] H. H. Shen, S. K. Fan, C. J. Kim, and D. J. Yao, "EWOD microfluidic systems for biomedical applications," *Microfluidics and Nanofluidics*, vol. 16, no. 5, pp. 965–987, 2014.

[29] M. G. Pollack, A. D. Shenderov, and R. B. Fair, "Electrowetting-based actuation of droplets for integrated microfluidics," *Lab on a Chip*, vol. 2, no. 2, 2002.

[30] V. Srinivasan, V. K. Pamula, and R. B. Fair, "An integrated digital microfluidic lab-on-a-chip for clinical diagnostics on human physiological fluids," *Lab on a Chip*, vol. 4, no. 4, 2004.

[31] P. Paik, V. K. Pamula, M. G. Pollack, and R. B. Fair, "Electrowetting-based droplet mixers for microfluidic systems," *Lab on a Chip*, vol. 3, no. 1, 2003.

[32] D. Chatterjee, B. Hetayothin, A. R. Wheeler, D. J. King, and R. L. Garrell, "Droplet-based microfluidics with nonaqueous solvents and solutions," *Lab on a Chip*, vol. 6, no. 2, pp. 199–206, 2006.

[33] A. R. Wheeler, H. Moon, C. A. Bird, R. R. Loo, C. J. Kim, J. A. Loo, and R. L. Garrell, "Digital microfluidics with in-line sample purification for proteomics analyses with MALDI-MS," *Analytical Chemistry*, vol. 77, no. 2, 2005.

[34] Y. H. Chang, G. B. Lee, F. C. Huang, Y. Y. Chen, and J. L. Lin, "Integrated polymerase chain reaction chips utilizing digital microfluidics," *Biomedical Microdevices*, vol. 8, no. 3, 2006.

[35] J. Chen, X. Xiong, L. Shui, Q. Zhang, H. Yang, and F. Zhang, "Enhanced dielectric constant and hydrophobicity of P(VDF–TrFE)-based composites," *Journal of Materials Science: Materials in Electronics*, vol. 29, no. 20, pp. 17 612–17 621, 2018. [Online]. Available: http://dx.doi.org/10.1007/s10854-018-9864-8

[36] Y. B. Sawane, S. B. Ogale, and A. G. Banpurkar, "Low Voltage Electrowetting on Ferroelectric PVDF-HFP Insulator with Highly Tunable Contact Angle Range," *ACS Applied Materials and Interfaces*, vol. 8, no. 36, pp. 24 049–24 056, 2016.

[37] S. N. Pei, "Light-Actuated Digital Microfluidics for Large-Scale Droplet Manipulation," 2011.

[38] S. Y. Park and P. Y. Chiou, "Light-driven droplet manipulation technologies for lab-on-a-chip applications," *Advances in OptoElectronics*, vol. 2011, no. 1, 2011.

[39] Hyundoo Hwang and Je-Kyun Park, "Optoelectrofluidic manipulation of nanoparticles and biomolecules," *Advances in OptoElectronics*, 2011.

[40] A. Manz, N. Graber, and H. M. Widmer, "Miniaturized total chemical analysis systems: A novel concept for chemical sensing," *Sensors and Actuators B: Chemical*, vol. 1, no. 1, pp. 244–248, 1990. [Online]. Available: http://www.sciencedirect.com/science/article/pii/092540059080209I

[41] S. A. Soper, A. C. Henry, B. Vaidya, M. Galloway, M. Wabuyele, and R. L. McCarley, "Surface modification of polymer-based microfluidic devices," *Analytica Chimica Acta*, vol. 470, no. 1, pp. 87–99, 2002.

[42] H. Becker and L. E. Locascio, "Polymer microfluidic devices," *Talanta*, vol. 56, no. 2, pp. 267–287, 2002.

[43] S. Ebnesajjad and P. R. Khaladkar, *Fluoropolymer Applications in the Chemical Processing Industries: The Definitive User's Guide and Databook*, second edi ed., ser. PDL handbook series, P. R. Khaladkar, Ed. Oxford, England ; Cambridge, Massachusetts : William Andrew, 2004.

[44] M. Vallet, B. Berge, and L. Vovelle, "Electrowetting of water and aqueous solutions on poly(ethylene terephthalate) insulating films," *Polymer*, vol. 37, no. 12, pp. 2465–2470, 1996.

[45] V. Narasimhan, S. Vijayavenkataraman, and S. Y. Park, "Low-cost spin-coatable, transferable, and high-K ion gel dielectric for flexible Electrowetting," *NSTI: Advanced Materials - TechConnect Briefs 2015*, vol. 3, no. June, pp. 230–233, 2015.

[46] S. Gu, H. Neugebauer, and N. S. Sariciftci, "Conjugated Polymer-Based Organic Solar Cells," pp. 1324–1338, 2007.

[47] J. Piris, T. E. Dykstra, A. A. Bakulin, P. H. Van Loosdrecht, W. Knulst, M. T. Trinh, J. M. Schins, and L. D. Siebbeles, "Photogeneration and ultrafast dynamics of excitons and charges in P3HT/PCBM blends," *Journal of Physical Chemistry C*, vol. 113, no. 32, pp. 14 500–14 506, 2009.

[48] S. F. Tedde, J. Kern, T. Sterzl, J. Fürst, P. Lugli, and O. Hayden, "Fully spray coated organic photodiodes," *Nano Letters*, vol. 9, no. 3, pp. 980–983, 2009.

[49] I. W. Hwang, D. Moses, and A. J. Heeger, "Photoinduced carrier generation in P3HT/PCBM bulk heterojunction materials," *Journal of Physical Chemistry C*, vol. 112, no. 11, pp. 4350–4354, 2008.

[50] D. E. Motaung, G. F. Malgas, S. S. Nkosi, G. H. Mhlongo, B. W. Mwakikunga, T. Malwela, C. J. Arendse, T. F. Muller, and F. R. Cummings, "Comparative study: The effect of annealing conditions on the properties of P3HT:PCBM blends," *Journal of Materials Science*, vol. 48, no. 4, pp. 1763–1778, 2013.

[51] B. Watts, W. J. Belcher, L. Thomsen, H. Ade, and P. C. Dastoor, "A quantitative study of PCBM diffusion during annealing of P3HT: PCBM blend films," *Macromolecules*, vol. 42, no. 21, pp. 8392–8397, 2009.

[52] X. Wang, O. Hofmann, R. Das, E. M. Barrett, A. J. DeMello, J. C. DeMello, and D. D. Bradley, "Integrated thin-film polymer/fullerene photodetectors for on-chip microfluidic chemiluminescence detection," *Lab on a Chip*, vol. 7, no. 1, pp. 58–63, 2007.

[53] D. Chen, A. Nakahara, D. Wei, D. Nordlund, and T. P. Russell, "P3HT/PCBM bulk heterojunction organic photovoltaics: Correlating efficiency and morphology," *Nano Letters*, vol. 11, no. 2, pp. 561–567, 2011.

[54] O. M. Ntwaeaborwa, R. Zhou, L. Qian, S. S. Pitale, J. Xue, H. C. Swart, and P. H. Holloway, "Post-fabrication annealing effects on the performance of P3HT:PCBM solar cells with/without ZnO nanoparticles," *Physica B: Condensed Matter*, vol. 407, no. 10, pp. 1631–1633, 2012. [Online]. Available: http://dx.doi.org/10.1016/j.physb.2011.09.103

[55] R. Cugola, U. Giovanella, P. Di Gianvincenzo, F. Bertini, M. Catellani, and S. Luzzati, "Thermal characterization and annealing effects of polythiophene/fullerene photoactive layers for solar cells," *Thin Solid Films*, vol. 511-512, pp. 489–493, 2006.

[56] S. Y. Loong, H. P. Lee, L. H. Chan, M.-S. Zhou, F. C. Loh, and K. L. Tan, "Characterization of polymer formation during SiO2 etching with different fluorocarbon gases (CHF3, CF4, C4F8)," in *Microelectronic Device Technology*,

M. Rodder, T. Tsuchiya, D. Burnett, and D. Wristers, Eds., vol. 3212, International Society for Optics and Photonics. SPIE, 1997, pp. 376–382. [Online]. Available: https://doi.org/10.1117/12.284614